bioRxiv preprint doi: https://doi.org/10.1101/2021.05.06.442926; this version posted May 7, 2021. The copyright holder for this preprint (which was not certified by peer review) is the author/funder, who has granted bioRxiv a license to display the preprint in perpetuity. It is made available under aCC-BY-NC-ND 4.0 International license.

Influenza A M2 recruits M1 to the plasma membrane: a fluorescence fluctuation microscopy study

Annett Petrich[1], Valentin Dunsing[1], Sara Bobone[2], Salvatore Chiantia[1*]

[1] University of Potsdam, Institute of Biochemistry and Biology, Karl-Liebknecht-Street 24-25, 14476 Potsdam, Germany

[2] University of Rome Tor Vergata, Department of Chemical Science and Technologies, Laboratory of Physical Chemistry, Via della Ricerca Scientifica 1, 00133 Roma

* Correspondence: chiantia@uni-potsdam.de

Abstract

Influenza A virus (IAV) is a respiratory pathogen that causes seasonal epidemics and occasional pandemics of severe illnesses with significant mortality. One of the most abundant proteins in IAV particles is the matrix protein 1 (M1), which is essential for the structural stability of the virus. M1 organizes virion assembly and budding at the plasma membrane (PM), where it can interact with other viral components and cellular membrane factors (i.e. lipids and host proteins). Of interest, the recruitment of M1 to the PM as well as its interaction with the other viral envelope proteins (hemagglutinin (HA), neuraminidase, matrix protein 2 (M2)) is controversially discussed in previous studies. Therefore, we used fluorescence fluctuation microscopy techniques (i.e. (cross-correlation) number and brightness, and scanning fluorescence cross-correlation spectroscopy) to quantify the oligomeric state of M1 and its interaction with other viral proteins in co-transfected as well as infected cells. Our results indicate that M1 is recruited to the PM by M2, as a consequence of the strong interaction between the two proteins. In contrast, only a weak interaction between M1 and HA was observed. M1-HA interaction occurred only in the case that M1 was already bound to the PM. We therefore conclude that M2 initiates the assembly of IAV by recruiting M1 to the PM, possibly allowing its further interaction with other viral proteins.

Keywords

fluorescence correlation spectroscopy, fluorescence fluctuation spectroscopy, fluorescence microscopy, hemagglutinin, influenza, matrix protein 1, matrix protein 2, neuraminidase, number and brightness, plasma membrane, protein-protein interaction, virus assembly

Abbreviations (nonstandard abbreviations, ≥ 3 times)

ACF, autocorrelation function; AF488, Alexa Fluor® 488; CCF, cross-correlation function; (cc)N&B, (cross-correlation) number and brightness; FP, fluorescence protein; HA, hemagglutinin protein; IAV, influenza A virus; M1, IAV matrix protein 1, M2, IAV matrix protein 2; mEGFP, monomeric enhanced green fluorescent protein; mp, myristoylated and palmitoylated; NA, neuraminidase protein; pf, fluorescence probability; PM, plasma membrane; sFCCS, scanning fluorescence cross-correlation spectroscopy; vRNPs, viral ribonucleoproteins

bioRxiv preprint doi: https://doi.org/10.1101/2021.05.06.442926; this version posted May 7, 2021. The copyright holder for this preprint (which was not certified by peer review) is the author/funder, who has granted bioRxiv a license to display the preprint in perpetuity. It is made available under aCC-BY-NC-ND 4.0 International license.

Introduction

Influenza A viruses (IAVs) belong to the family of the *Orthomyxoviridae*. These pathogens represent a substantial global health burden, being associated with significant morbidity and mortality through frequent epidemics and several pandemics [1, 2]. IAV is enveloped by a lipid bilayer that is derived from the host cell membrane and contains two integral transmembrane glycoproteins (i.e. hemagglutinin (HA) and neuraminidase (NA)) and one transmembrane protein with a proton-selective ion channel activity (i.e. the matrix protein 2 (M2)) [3, 4]. The envelope protein HA is a homotrimeric type I transmembrane glycoprotein and is the major surface protein of IAV particles [5-7]. HA plays a major role in viral entry by mediating the attachment of the virus to cell surface sialic acid molecules, membrane fusion after internalization, and the release of viral genome into target cells [5-8]. The surface protein NA is a homotetrameric type II transmembrane glycoprotein that facilitates the release of newly synthesized virus particles from the infected cells by enzymatic cleavage of the cell surface receptor molecules [5-8]. Additionally, a small amount of homotetrameric M2 molecules are embedded in the viral envelope (approximately 16 to 20 molecules in a virus, compared to ca. 300-400 HA and 50 NA copies) [6, 7]. M2 is a type III transmembrane protein which functions as proton channel activated by acidic pH and is important for genome unpacking during virus entry [7-9]. Moreover, it was shown that M2 is connected to virus morphology, production of infectious virus particles, and membrane scission [9-13]. All the three envelope proteins are transported from the trans-Golgi network to the apical plasma membrane via the secretory pathway [8, 9, 14]). Both glycoproteins, HA and NA, are supposed to be enriched in lipid “raft” microdomains at the virion budding site, whereas M2 was suggested to localize to the edges of such domains [8, 14-16].

The luminal side of the viral envelope is coated with the matrix protein 1 (M1), which forms the viral nucleocapsid in close contact to the lipid membrane [17-20], binds the viral ribonucleoproteins (vRNPs) [4, 21], and is supposed to interact with viral surface proteins [10, 11, 22-24]. Moreover, M1 is the most abundant, highly conserved protein in IAV particles and is important for several processes during viral replication, including the regulation of capsid disassembly, virus budding and morphogenesis [3, 8, 25]. Interestingly, M1 lacks an apical transport signal, implying that the membrane localization of M1 in infected cells might be due to piggyback transport with HA, NA, M2 or vRNPs [26, 27]. For

bioRxiv preprint doi: https://doi.org/10.1101/2021.05.06.442926; this version posted May 7, 2021. The copyright holder for this preprint (which was not certified by peer review) is the author/funder, who has granted bioRxiv a license to display the preprint in perpetuity. It is made available under aCC-BY-NC-ND 4.0 International license.

this reason, various hypotheses regarding the association of M1 to the plasma membrane (PM) have been proposed over the years. First, several studies established that M1 associates with negatively charged lipids in model membranes [17-20, 28, 29]. Nevertheless, such interactions appear not to be sufficient for the actual association of M1 to the PM in non-infected cells (i.e. in cells expressing M1 as the only viral protein) [17, 27]. Accordingly, M1 was shown to interact with the cytoplasmic tails of HA and NA during their apical transport [22-24, 30, 31], as well as with the cytoplasmic tails of M2 at the assembly site [10, 11, 27]. Interactions between M1 and HA, NA, or M2 have been only demonstrated indirectly (e.g. by altered detergent solubility [22, 24], increased membrane association [31] of M1 in the presence of HA or NA, or co-immunoprecipitation of M1 in the presence of M2 [10, 11, 32]). Several reports showed contradicting data regarding HA/NA-M1 interactions [33-36] as well as the recruitment of M1 to the PM by M2 [37, 38]. In conclusion, the molecular mechanisms involved in M1-driven IAV assembly are not fully understood and the specific interactions between M1 and other viral surface proteins have not yet been clarified directly in living cells.

To obtain quantitative information on how protein-protein interactions (e.g. M1-M1 or M1-HA) occur in the native cellular environment, minimally invasive approaches (e.g. fluorescence fluctuation spectroscopy) are needed [39]. Here, we apply (cross-correlation) Number and Brightness ((cc)N&B) as well as scanning fluorescence cross-correlation spectroscopy (sFCCS) analysis in living cells to quantify the oligomeric state, concentration and the diffusion dynamics of the viral envelope proteins (HA, NA, M2) and M1, as well as their interactions. Our results suggest the presence of a strong interaction between M1 and M2, leading to the recruitment of M1 to the PM in a M2 concentration-dependent manner. We further hypothesize that the interaction between M1 and HA occurs in a subsequent step. Finally, we provide the first experimental evidence of a possible M2 binding-site within the N-terminal domain of M1.

bioRxiv preprint doi: https://doi.org/10.1101/2021.05.06.442926; this version posted May 7, 2021. The copyright holder for this preprint (which was not certified by peer review) is the author/funder, who has granted bioRxiv a license to display the preprint in perpetuity. It is made available under aCC-BY-NC-ND 4.0 International license.

Materials and Methods

Plasmids and cloning.

The plasmids for the transcription and translation of influenza virus RNAs and proteins of the influenza A/FPV/Rostock/1934 virus (H7N1; FPV) mutant 1 were obtained from Michael Veit (Free University, Berlin, Germany), and previously described [40, 41]. The plasmids encoding the fluorescence proteins (FP) EGFP or mCherry2 linked to a myristoylated and palmitoylated peptide (mp-mEGFP, mp-mCherry2, mp-2x-mEGFP), and the plasmids for cytosolic expression of mEGFP, 2x-mEGFP were previously described [42] and are available on Addgene (Watertown, MA, USA). The plasmids encoding the FP hetero-dimer mCherry2-mEGFP linked to a myristoylated and palmitoylated peptide (mp-mCherry2-mEGFP), and the matrix protein 2 (M2) of FPV with mCherry2 fused to the extracellular terminus of M2 (mCherry2-M2) were previously described [43].

For the cloning of all following constructs, standard PCRs with custom-designed primers were performed, followed by digestion with FastDigest restriction enzymes and ligation with T4-DNA-Ligase according to the manufacturer's instructions. All enzymes and reagents were purchased from Thermo Fisher Scientific (Waltham, MA, USA) and primers were acquired from Sigma Aldrich trademark of Merck KGaA (Darmstadt, Germany). The accuracy of each construct was verified by Sanger sequencing (LGC Genomics GmbH, Berlin, Germany).

The original plasmid encoding FPV matrix protein 1 (M1) with EYFP fused to the N-terminus or C-terminus of M1 (EYFP-M1, M1-EYFP) was a kind gift of Michael Veit (Free University, Berlin, Germany), and previously described [44]. A monomeric variant of EGFP, containing the A206K mutation [45], was inserted into both M1 constructs by digestion of mEGFP-C1 (gift from Michael Davidson, Addgene plasmids #54759) with AgeI and BsrGI. The modification of M1-mEGFP with an N-terminal mp-signal (amino acids MGCIKSKRKDNLNDDEPV, mp-M1-mEGFP) or an N-terminal mp-signal with an additional polybasic sequence (amino acids MGCIKSKRKDGKKFWKRLRKFLRKLKS, mp-KrΦ-M1-mEGFP) were introduced by PCR with primers encoding the additional amino acids. For the construction of mp-M1-mEGFP and mp-KrΦ-M1-mEGFP, the PCR products were subcloned into mEGFP-N1 (gift from Michael Davidson, Addgene plasmid #54767) with XhoI and EcoRI. The truncated M1 sequences encoding the M1 N-terminus (NM1, amino acids 1–67; 1-86; 1-

bioRxiv preprint doi: https://doi.org/10.1101/2021.05.06.442926; this version posted May 7, 2021. The copyright holder for this preprint (which was not certified by peer review) is the author/funder, who has granted bioRxiv a license to display the preprint in perpetuity. It is made available under aCC-BY-NC-ND 4.0 International license.

164) or the M1 C-terminus (CM1, amino acids 165–252) were amplified from the plasmid M1-mEGFP, and subcloned into mEGFP-N1 by using the restriction endonucleases XhoI and EcoRI, yielding plasmids NM1(1-67)-mEGFP, NM1(1-86)-mEGFP, NM1(1-164)-mEGFP, and CM1(165-252)-mEGFP.

An untagged FPV M2 construct was cloned by amplifying M2 sequence from FPV-M2-EYFP (a kind gift from Michael Veit), and cloned into pcDNA3.1+ (Thermo Fisher Scientific, Waltham, MA, USA , #V79020) via restriction with HindIII and EcoRI. The plasmid for bi-directional expression was a gift from Katja Arndt (University of Potsdam, Potsdam, Germany) and has the two promoters TTC31 and CCDC142, allowing for simultaneous expression of the encoded genes [46]. For the calibration of the relative expression level, mp-EGFP and mp-mCherry2 were amplified and cloned into the two expression cassettes flanked by restriction sites BamHI/EcoRI and SacI/KpnI respectively, to obtain mp-mEGFP ↔ mp-mCherry2. A construct with mp-mCherry2 and mp-mEGFP cloned into BamHI/EcoRI and SacI/KpnI restriction sites, respectively, was also produced (mp-mCherry2 ↔ mp-mEGFP). Unlabeled M2 sequence was amplified and separately cloned into the BamHI/EcoRI cassette to produce M2 ↔ mp-mCherry2. Site-directed mutagenesis in order to replace the amino acids of the M1-binding site in M2 (amino acids 71–73, SMR) by alanine residues was performed by two-step overlap-extension PCR of the plasmid mCherry2-M2, yielding the plasmid mCherry2-$M2_{mut}$.

The FPV HA constructs HA_{wt}-mCherry2 and mCherry2-HA_{TMD} were cloned based on the previously described HA_{wt}-mEGFP [42] and mEGFP-HA_{TMD} [42] plasmids. HA_{wt}-mEGFP contains full-length HA protein fused to mEGFP at the (intracellular) C-terminus, whereas in mEGFP -HA_{TMD} a large part of the extracellular domain of HA is replaced by mEGFP. To clone mCherry2-HA_{TMD} and HA_{wt}-mCherry2, the mEGFP-HA_{TMD}, HA_{wt}-mEGFP, and mCherry2-C1 plasmids [42] were digested with AgeI and BsrGI to replace mEGFP with mCherry2.

The FPV neuraminidase (NA) construct was cloned by amplifying NA sequence from pHH21-NA [41], and cloned into pcDNA3.1+ (Thermo Fisher Scientific, Waltham, MA, USA , #V79020) via restriction with NheI and AflII. To clone NA-mCherry2, mCherry2 was amplified from mCherry2-C1, and the obtained insert was ligated into NA-pcDNA3.1+ by digestion with NotI and XbaI. The construct contains full-length NA fused to mCherry2 at the extracellular side.

bioRxiv preprint doi: https://doi.org/10.1101/2021.05.06.442926; this version posted May 7, 2021. The copyright holder for this preprint (which was not certified by peer review) is the author/funder, who has granted bioRxiv a license to display the preprint in perpetuity. It is made available under aCC-BY-NC-ND 4.0 International license.

Cell culture.

Human embryonic kidney (HEK) cells from the 293T line (CRL-3216TM, purchased from ATCC®, Kielpin Lomianki, Poland), and Madin-Darby canine kidney type II (MDCK II) cells (ECACC 00062107, European Collection of Authenticated Cell Cultures, Porton Down, UK) were cultured in phenol red-free Dulbecco's modified Eagle medium (DMEM) with 10 % fetal bovine serum, 2mM L-glutamine, 100 U/mL penicillin, and 100 µg/mL streptomycin at 37 °C and 5 % CO_2. Cells were passaged every 2-3 days when they reached nearly 80% confluence in tissue culture flask, for no more than 15 times. All solutions, buffers, and media used for cell culture were purchased from PAN-Biotech (Aidenbach, Germany).

For immunostaining experiments, dishes were coated with a 0.01 % (w/v) poly-L-lysine solution (MW 150,000 – 300,000 Da, Sigma-Aldrich, Munich, Germany) before cell seeding.

Virus propagation and titration.

For virus propagation, confluent MDCK II cells were infected with the avian influenza A/FPV/Rostock/1934 virus mutant 1 (kind gift from Michael Veit, Free University Berlin [40]) at MOI 0.01 in DMEM with 0.2 % (w/v) Bovine Serum Albumin (BSA; Sigma Aldrich, Taufkirchen, Germany), 1 mM L-glutamine, 100 U/mL penicillin, and 100 µg/mL streptomycin and incubated at 37 °C. After one hour, virus inoculum was removed and the cells were washed twice with Dulbecco's phosphate-buffered saline with Mg^{2+}/Ca^{2+} (DPBS+/+; PAN-Biotech, Aidenbach, Germany). Fresh infection medium with 0.1 µg/mL TPCK-treated trypsin (Sigma Aldrich, Taufkirchen, Germany) was added to the cells and incubated for 2-3 days at 37 °C. Upon visual observation of a cytopathic effect, the supernatant was harvested and cellular debris was removed by centrifugation (3000 x *g* for 30 min at 4 °C). Virus aliquots were stored at -80 °C.

To measure the plaque-forming units (PFU) of the suspension, MDCK II cells were grown in six-well plates until full confluency was reached. The cells were infected with serial 10-fold dilutions of the virus containing supernatant and incubated for one hour at 37°C. Virus inoculum was then removed and replaced by SeaPlaque agarose overlay medium (1x MEM (PAN-Biotech, Aidenbach, Germany), 0.9 % (w/v) SeaPlaque Agarose (Biozym Scientific GmbH, Hessisch Oldendorf, Germany), 0.2 % (w/v) Bovine Serum Albumin, 1 mM L-

bioRxiv preprint doi: https://doi.org/10.1101/2021.05.06.442926; this version posted May 7, 2021. The copyright holder for this preprint (which was not certified by peer review) is the author/funder, who has granted bioRxiv a license to display the preprint in perpetuity. It is made available under aCC-BY-NC-ND 4.0 International license.

glutamine, 100 U/mL penicillin, and 100 µg/mL streptomycin). After three days of incubation at 37 °C and 5 % CO2, agarose overlay medium was removed, cells were fixated with 10 % (w/v) formaldehyde (Sigma Aldrich, Taufkirchen, Germany) for one hour and PFU was determined by crystal violet staining (0.05 % (w/v) crystal violet (Sigma Aldrich, Taufkirchen, Germany), 1 % (w/v) formaldehyde, 1 % (v/v) methanol in 1 x PBS) [47].

Transfection and virus infection.

Cells were seeded in 35-mm dishes (CellVis, Mountain View, CA, USA) with an optical glass bottom (#1.5 glass, 0.16–0.19 mm) at a density of 6×10^5 cells per dish. After 24 h, cells were transfected with Turbofect® according to the manufacturer's instructions (Thermo Fisher Scientific, Waltham, MA, USA) by using 200 ng pDNA per dish for the controls or 600 - 1200 ng pDNA per dish for IAV proteins. Briefly, plasmids were incubated for 20 min with 3 µL Turbofect diluted in 50 µL serum-free medium, and then added dropwise to the cells.

When needed, cells were co-transfected with the reverse genetic plasmid set of FPV except for segment 7 (encoding M). Instead of segment M, M1-mEGFP and M2-untagged were used. This co-transfection procedure is referred to in what follows as "all".

In some cases, cells were infected with a multiplicity of infection (MOI) 5 with IAV FPV mutant 1 in infection medium at 5 h post-transfection, first on ice for 15 min and then at 37°C for 45 min. Samples were then rinsed with DPBS+/+ and typically observed 12 to 16 h after infection.

Immunofluorescence.

Transfected and infected cells were fixed at the indicated time points with 4 % (w/v) Paraformaldeyde (Sigma Aldrich, Taufkirchen, Germany) in DPBS+/+. After 15 min, cells were washed three times with DPBS+/+. Permeabilization was performed with 0.1 % (v/v) Triton X-100® (Sigma Aldrich, Taufkirchen, Germany) for 10 min, and subsequently washed three times with DPBS+/+. Afterwards, cells were incubated with 2 % (w/v) BSA (Sigma Aldrich, Taufkirchen, Germany) in DPBS+/+ for one hour at room temperature. Primary antibody (monoclonal mouse anti-influenza A matrix protein 2, clone 14C2 (#ab5416, abcam, Cambridge, UK) or monoclonal mouse anti-influenza nucleoprotein, clone A1 (#MAB8257, Millipore trademark of Merck KGaA, Darmstadt,Germany)) were diluted 1:200 or 1:1000 in

bioRxiv preprint doi: https://doi.org/10.1101/2021.05.06.442926; this version posted May 7, 2021. The copyright holder for this preprint (which was not certified by peer review) is the author/funder, who has granted bioRxiv a license to display the preprint in perpetuity. It is made available under aCC-BY-NC-ND 4.0 International license.

0.2 % (w/v) BSA in DPBS+/+, and incubated overnight at 4 °C. After three washing steps with DPBS+/+, cells were incubated with the 1:1000 diluted secondary antibodies (goat anti-mouse AlexaFluor® 488-conjugated; Thermo Fisher Scientific, Waltham, MA, USA) for one hour at room temperature. Cells were subsequently washed three times with DPBS+/+.

Confocal microscopy imaging.

Microscopy measurements were performed on a Zeiss LSM780 system (Carl Zeiss, Oberkochen, Germany) using a Plan-Apochromat 40×/1.2 Korr DIC M27 water immersion objective and a 32-channel GaAsP detector array. To decrease out-of-focus light, a pinhole size of one airy unit (~39 µm) was used. Samples were excited with a 488-nm argon laser and a 561-nm diode laser. Fluorescence was detected between 499 and 570 nm (mEGFP, AlexaFluor®488) and between 590 and 695 nm (mCherry2), after passing through a MBS 488/561-nm dichroic mirror. For multicolour measurements, fluorophores were excited and detected sequentially for different regions of the spectrum. Confocal imaging was performed with a frame size of 512 x 512 pixels.

Confocal microscopy system and setup calibration for fluorescence fluctuation spectroscopy.

All fluorescence fluctuation spectroscopy measurements were performed on a Zeiss LSM780 system (Carl Zeiss, Oberkochen, Germany) using a Plan-Apochromat 40×/1.2 Korr DIC M27 water immersion objective and a 32-channel GaAsP detector array. Samples were excited with a 488 nm Argon laser (AlexaFluor®488, mEGFP) and a 561 nm diode laser (mCherry2). For measurements with 488 nm excitation, fluorescence was detected between 499 and 552 nm; for 561 nm excitation, between 570 and 695 nm, after passing through a 488/561 nm dichroic mirror (for two color measurements) or 488 nm dichroic mirror (for one color measurements). All measurements with more than one fluorescent species were recorded sequentially to minimize signal cross-talk. To decrease out-of-focus light, a pinhole size of one airy unit (~39 µm) was used. All measurements were performed at room temperature (22 ± 1 °C).

At the beginning of each measurement day, the focal volume was calibrated by performing a series of point FCS measurements with Alexa Fluor® 488 (AF488, Thermo Fischer, Waltham,

bioRxiv preprint doi: https://doi.org/10.1101/2021.05.06.442926; this version posted May 7, 2021. The copyright holder for this preprint (which was not certified by peer review) is the author/funder, who has granted bioRxiv a license to display the preprint in perpetuity. It is made available under aCC-BY-NC-ND 4.0 International license.

MA, USA) dissolved in water at 30 nM, at the same laser power, with the same dichroic mirror and pinhole size. Beforehand, the signal was optimized by adjusting the collar ring of the objective and the pinhole position to the maximal count rate for AF488. Then, ten measurements at different locations were taken, each consisting of 15 repetitions of 10 s, and the data were fitted using a three-dimensional diffusion model including a triplet contribution. The structure parameter S (defined as the ratio between the vertical and lateral dimension of the theoretical confocal ellipsoid) was typically around 5 to 9, and the diffusion time τ_d around 35 to 40 µs. The waist ω_0 was calculated from the measured average diffusion time ($\tau_{d,AF488}$) and previously determined diffusion coefficient D of the used dye at room temperature (D_{AF488}= 435 µm^{2}s^{-1}) [48], according to the following equation:

$$\omega_0 = \sqrt{4\tau_{d,AF488}D_{AF488}} \quad (1)$$

Typical values were 200–250 nm. All measurements were performed at room temperature.

Scanning fluorescence (cross-) correlation spectroscopy.

Scanning fluorescence correlation spectroscopy (sFCS) and fluorescence cross-correlation spectroscopy (sFCCS) to probe slow diffusive dynamics in lipid membranes were performed as previously described [39, 42, 49-52] with few modifications. Briefly, a line scan of 256 × 1 pixels (pixel size 80 nm) was performed perpendicular to the membrane with 472.73 µs scan time. Typically, 250,000 lines were acquired (total scan time 3 min) in photon counting mode. Laser powers were adjusted to keep photobleaching below 20%. Typical values were ~4.7 µW (488 nm) and ~10 µW (561 nm). Scanning data were exported as TIFF files, imported and analyzed in MATLAB (The MathWorks, Natick, MA, USA) using custom-written code. The analysis started with an alignment of all lines as kymographs and then a division into blocks of 1000 lines. In each block, lines were summed up column-wise and the position along the line with maximum fluorescence was determined. This position defines the membrane localization in each block and is used to align all lines to a common origin. Then, all aligned line scans were averaged over time and fitted with a Gaussian function summed to a sigmoidal function (modelling intra-cellular background signal). The pixels corresponding to the membrane were defined as pixels within ±2.5σ of the peak. To clearly identify the signal originating from the PM, we restricted our analysis to cells in which the surface

bioRxiv preprint doi: https://doi.org/10.1101/2021.05.06.442926; this version posted May 7, 2021. The copyright holder for this preprint (which was not certified by peer review) is the author/funder, who has granted bioRxiv a license to display the preprint in perpetuity. It is made available under aCC-BY-NC-ND 4.0 International license.

concentration of the analyzed FP was > 100 monomers/µm². In each line, these pixels were integrated, providing the membrane fluorescence time series *F(t)*. In order to correct for depletion due to photobleaching, the fluorescence time series was fitted with a two-component exponential function and a correction was applied [53]. Then, autocorrelation functions (ACFs; g= green channel, r =red channel), and cross-correlation function (CCF) were calculated as follows, using a multiple tau algorithm:

$$G_i(\tau) = \frac{<\delta F_i(t)\delta F_i(t+\tau)>}{<F_i(t)>^2}, \tag{2}$$

$$G_{cross}(\tau) = \frac{<\delta F_g(t)\delta F_r(t+\tau)>}{<F_g(t)><F_r(t)>}, \tag{3}$$

where $\delta F_i = F_i(t) - < F_i(t) >$ and $i = g, r$.

To avoid artefacts caused by long-term instabilities or single bright events, CFs were calculated segment-wise (20 segments) and then averaged. Segments showing clear distortions (typically less than 25% of all segments) were manually removed [39]. Furthermore, a model for two-dimensional diffusion in the membrane and a Gaussian confocal volume geometry was fitted to the ACFs and CCF [52]:

$$G(\tau) = \frac{1}{N}\left(1 + \frac{\tau}{\tau_d}\right)^{-1/2}\left(1 + \frac{1}{S^2\tau_d}\right)^{-1/2}. \tag{4}$$

Here, the particle number N and diffusion time τ_d were obtained from the fit. Moreover, diffusion coefficients (D) were calculated using the calibrated waist ω_0 of the focal volume, $D = \omega_0^2/4\tau_d$. The molecular brightness ε was calculated by dividing the mean count rate detected for each species *i*, $< F_i(t) >$, by the particle number N_i determined from the fit:

$$\varepsilon_i = \frac{<F_i(t)>}{N_i}. \tag{5}$$

Relative cross-correlation values were calculated from the amplitudes of ACFs and CCFs:

$$rel.cc = max\left\{\frac{G_{cross}(0)}{G_g(0)}, \frac{G_{cross}(0)}{G_r(0)}\right\}, \tag{6}$$

where $G_{cross}(0)$ is the amplitude of the CCF and $G_i(0)$ is the amplitude of the ACF in the *i*-th channel (g = green, r = red) [39].

bioRxiv preprint doi: https://doi.org/10.1101/2021.05.06.442926; this version posted May 7, 2021. The copyright holder for this preprint (which was not certified by peer review) is the author/funder, who has granted bioRxiv a license to display the preprint in perpetuity. It is made available under aCC-BY-NC-ND 4.0 International license.

To analyze concentration-dependent oligomerization, the surface concentration was calculated according to the following equations:

$$N_{monomer,protein} = \frac{<I_{protein}>}{\varepsilon_{monomer,i}}, \quad (7)$$

$$surface\ concentration = \frac{N_{monomer,protein}}{p_{f,i}\pi\omega_0^2 S}, \quad (8)$$

where $< I_{protein} >$ is the average fluorescence intensity of the protein of interest within a single cell measurement, $\varepsilon_{monomer,i}$ is the average molecular brightness of the monomer control for the corresponding fluorescence species *i*, and $p_{f,i}$ is the probability factor described below in "Brightness calibration and fluorophore maturation". By using the effective detection area ($A_{eff} = \pi\omega_0^2 S$), the surface concentration for a protein of interest in expressed in monomeric units per µm^2.

(Cross-Correlation) Number and Brightness.

(Cross-correlation) Number and Brightness ((cc)N&B) experiments were performed as previously described [39, 42, 50, 54, 55] with few modifications. Briefly, an image stack was acquired over time at a fixed position in the sample, typically consisting of 100 frames. Images of 128 x 512 pixels were acquired by using a pixel size of 70 nm, and 6.3 µs dwell time. In order to account for the slow dynamics of clusters, a 5 s break was introduced between each frame. Laser powers were maintained low enough to keep bleaching below 20 % of the initial fluorescence signal (typically ~3 µW for 488 nm, and ~5 µW for 561 nm). CZI image output files were imported into MATLAB using the Bioformats package [56], and analyzed using a self-written MATLAB script implementing the equations from Digman et al. [57] for the specific case of photon-counting detectors, thus obtaining the molecular brightness and number as a function of pixel position. Before further analysis, pixels corresponding to regions of interest (ROI) were selected manually in an image map. To clearly identify the signal originating from the PM, we restricted our analysis to cells in which the surface concentration of the analyzed FP was > 100 monomers/µm². Next, to correct for lateral drift during the acquisition, frames were aligned to the first frame by maximizing the spatial correlation between sub-selections in consecutive frames, averaged over both

bioRxiv preprint doi: https://doi.org/10.1101/2021.05.06.442926; this version posted May 7, 2021. The copyright holder for this preprint (which was not certified by peer review) is the author/funder, who has granted bioRxiv a license to display the preprint in perpetuity. It is made available under aCC-BY-NC-ND 4.0 International license.

channels, as a function of arbitrary translations [58]. Finally, brightness-intensity maps were obtained (see e.g. Figure 2 B). These maps show the pixel brightness with a color code in units of counts/dwell time/molecule. The average fluorescence count rate (counts/dwell time) is represented as pixel intensity.

Corrections for bleaching, minor cell movements and specific detector response were performed as described in [39, 55]. The calculation of the multimerization state from brightness values is described below in the paragraph "Brightness calibration and fluorophore maturation".

Finally, for two color measurements, the cross variance $\sigma_{cc}^2 =< \left(I_g -< I_g >\right)(I_r -< I_r >) >$ was calculated for each pixel [54]. In order to obtain a ccN&B analogue of Eq. 6, we defined:

$$N_{cc} = \frac{\sigma_{cc}^2}{\varepsilon_g \varepsilon_r}, \tag{9}$$

where ε_i is the channel brightness ($i = g, r$) calculated as usual as $\frac{\sigma_i^2}{<I_i>} - 1$.

The relative cross-correlation values were calculated in analogy to Eq. 6 from the particle numbers for each channel N_i ($i = g, r$; $N_i = \frac{<I_i>}{\varepsilon_i}$), and the apparent number of complexes N_{cc}:

$$rel.cc. = max\left\{\frac{N_{cc}}{N_g}, \frac{N_{cc}}{N_r}\right\}. \tag{10}$$

To analyze concentration-dependent oligomerization, the surface concentration was calculated according Eqs. 7 and 8.

Brightness calibration and fluorophore maturation

The molecular brightness, i.e. the photon count rate per molecule, is used as a measure for the oligomeric state of protein complexes. This quantity is often based on the assumption that all fluorophores within an oligomer are fluorescent. However, fluorescent proteins can undergo dark state transitions or be in a non-mature, non-fluorescent state [59]. To quantify the amount of non-fluorescent FPs, we consider all these processes together in a single parameter, the apparent fluorescence probability (p_f), i.e. the probability of a FP to emit a

bioRxiv preprint doi: https://doi.org/10.1101/2021.05.06.442926; this version posted May 7, 2021. The copyright holder for this preprint (which was not certified by peer review) is the author/funder, who has granted bioRxiv a license to display the preprint in perpetuity. It is made available under aCC-BY-NC-ND 4.0 International license.

fluorescence signal. We used the median of the normalized FP homo-dimer brightness ε_{dimer} to determine the probability *pf* for each FP species *i*:

$$pf_i = \frac{<\varepsilon_{i,dimer}>}{<\varepsilon_{i,monomer}>} - 1. \quad (11)$$

(11)

An estimate of the oligomeric state is determined by normalizing the molecular brightness ε_i by the average molecular brightness $\varepsilon_{i,mono}$ of the corresponding monomeric reference and, subsequently, using the previously determined values of $p_{f,i}$ for species *i* [42]:

$$\text{Oligomerization}=\frac{1}{p_{f,i}}\left(\frac{\varepsilon_i}{\varepsilon_{i,monomer}} - 1\right) + 1. \quad (12)$$

We applied this transformation to every brightness data point of both (cc)N&B and sF(C)CS measurements, obtaining then the true oligomeric size of the complexes.

Calibration of bi-directional plasmids

We examined bi-directional plasmids with either i) mp-mEGFP upstream and mp-mCherry2 downstream of the bi-directional promoter region (mp-mEGFP ↔ mp-mCherry2) or ii) mp-mCherry2 upstream and mp-mEGFP downstream of the bi-directional promoter region (mp-mCherry2 ↔ mp-mEGFP). sFCS measurements were independently performed at the membrane of transfected HEK293T cells (Figure S1 A) to calculate the concentrations of each FP, for each bidirectional plasmid. The box plot (Figure S1 B) with the single data points for each experiment shows the expression ratio, defined as the ratio between the measured amounts of FPs (downstream and upstream of the promoter region). Each FP amount is quantified as the number of molecules detected in the confocal volume, provided by sFCCS. The expression ratio for mp-mEGFP ↔ mp-mCherry2 was then used to estimate the concentration of M2 for the experiments in which the M2 ↔ mCherry2 construct was used for transfection.

Statistical analysis.

Data from at least three independent experiments were pooled and visualized by using GraphPad Prism vs. 9.0.0 (GraphPad Software, LCC, San Diego, CA, USA) or R (R Foundation for Statistical Computing, Vienna, Austria) packages *ggplot2* [60], *ggpubr* [61], and *cowplot*

bioRxiv preprint doi: https://doi.org/10.1101/2021.05.06.442926; this version posted May 7, 2021. The copyright holder for this preprint (which was not certified by peer review) is the author/funder, who has granted bioRxiv a license to display the preprint in perpetuity. It is made available under aCC-BY-NC-ND 4.0 International license.

[62]. If not otherwise indicated, data were displayed as box plots with single data points corresponding to measurements in single cells. Median values and whiskers ranging from minimum to maximum values are displayed. Quantities in the main text are given as median ± IQR. Sample sizes and p-values are given in each graph and figure captions, respectively. Statistical significance was tested by using D`Agostino-Pearson normality test followed by the one-way ANOVA analysis and the Bonferroni's multiple comparisons test.

Code availability.

MATLAB custom-written code is available from the corresponding author upon reasonable request.

Data availability.

The datasets analyzed during the current study are available from the corresponding author upon reasonable request.

bioRxiv preprint doi: https://doi.org/10.1101/2021.05.06.442926; this version posted May 7, 2021. The copyright holder for this preprint (which was not certified by peer review) is the author/funder, who has granted bioRxiv a license to display the preprint in perpetuity. It is made available under aCC-BY-NC-ND 4.0 International license.

Results

M1 is recruited to the PM by M2 but not by HA or NA

Previous studies have shown that the intracellular localization of the Influenza A matrix protein M1 varies between transfected and infected cells [15, 27]. As a starting point for our investigations, we have therefore characterized the behavior of a M1-mEGFP fluorescent construct derived from the avian IAV strain FPV directly in living HEK293T cells. Protein localization was monitored via confocal microscopy either i) when expressed by itself, ii) in the presence of all other viral proteins (i.e., via the reverse genetic plasmid system termed here as “all”), or iii) in FPV infected cells (Figure 1).

Expression of M1-mEGFP alone indicated a homogenous distribution of M1 through the cytosol and the nucleus (Figure 1 A), whereas mEGFP-M1 (i.e., mEGFP fused at the N-terminus) formed large, bright aggregates in the cytosolic region in close proximity to the nucleus (data not shown). The localization of M1-mEGFP was similar to what was previously described for unlabeled M1 [44, 63]. Therefore, this construct was used for all further experiments. Upon co-transfection of all other IAV (unlabeled) proteins, a distinct enrichment of M1-mEGFP at the PM was detectable, with the protein being homogeneously distributed (Figure 1 A). A statistical analysis of the frequency of such an occurrence is not trivial since the amount of cells effectively transfected with all 9 plasmids is unknown and might be extremely low (roughly estimated to be < 5%, considering the data reported by Hoffmann et al. [64] and assuming that the probability of transfection with each plasmid is the same and does not increase with the addition of further plasmids). Notably, we observed filamentous structures originating from the PM (Figure 1B, left) that were not present when M1 was substituted by the membrane-anchored mp-mEGFP (data not shown). Cells infected with FPV showed heterogeneous M1 binding to the PM and formation of clusters in almost every cell (i.e. >90%) at 24 hpi (Figure 1 A), as previously observed also for unlabeled M1 [15, 16]. M1-enriched filamentous structures at the PM were even more evident, compared to the case of the reverse genetic plasmid system (Figure 1 B, right). The effectiveness of IAV infection was confirmed via immunofluorescence detection of expressed nucleoprotein (ca. 90% of infected cells, data not shown).

bioRxiv preprint doi: https://doi.org/10.1101/2021.05.06.442926; this version posted May 7, 2021. The copyright holder for this preprint (which was not certified by peer review) is the author/funder, who has granted bioRxiv a license to display the preprint in perpetuity. It is made available under aCC-BY-NC-ND 4.0 International license.

In order to determine whether M1 localization is determined by the presence of other viral proteins at the PM as previously suggested [15, 16], M1-mEGFP was co-expressed with either mCherry2-M2, mCherry2-HA_{TMD}, or NA-mCherry2 (Figure 1 C-E). It is worth noting that these viral proteins are labeled at the extracellular side (so to preserve possible interactions with intracellular M1) and strongly localize at the PM, similarly to their non-fluorescent counterparts [65, 66]. Fluorescence microscopy imaging indicated the absence of M1-mEGFP localization at the PM in cells co-expressing this protein with mCherry2-HA_{TMD}, NA-mCherry2 constructs (Figure 1 D-E) or unlabeled HA (data not shown). On the other hand, upon a co-expression of M1-mEGFP with mCherry2-M2, clear colocalization of both proteins at the PM was observed (Figure 1 C). Unequivocable association of M1-mEGFP to the PM was observed in circa one quarter of the examined cells and appeared qualitatively correlated with the amount of mCherry2-M2 at the PM (data not shown). A quantitative analysis of the correlation between the concentrations of the two proteins at the PM is presented in the following paragraphs. The membrane distribution of M1-mEGFP was mostly homogeneous and no filamentous structures or clustering of M1-mEGFP at the PM were detectable. M2-induced binding of M1-mEGFP to the PM was qualitatively not further influenced by co-expression of mCherry2-HA_{TMD} or NA-mCherry2 (Figure 1 D-E).

In conclusion, M2 seems to be necessary for the recruitment of M1 to the PM. Also, the lateral organization of this protein on the lipid membrane is influenced by the presence of other viral proteins, as observed in infected cells.

bioRxiv preprint doi: https://doi.org/10.1101/2021.05.06.442926; this version posted May 7, 2021. The copyright holder for this preprint (which was not certified by peer review) is the author/funder, who has granted bioRxiv a license to display the preprint in perpetuity. It is made available under aCC-BY-NC-ND 4.0 International license.

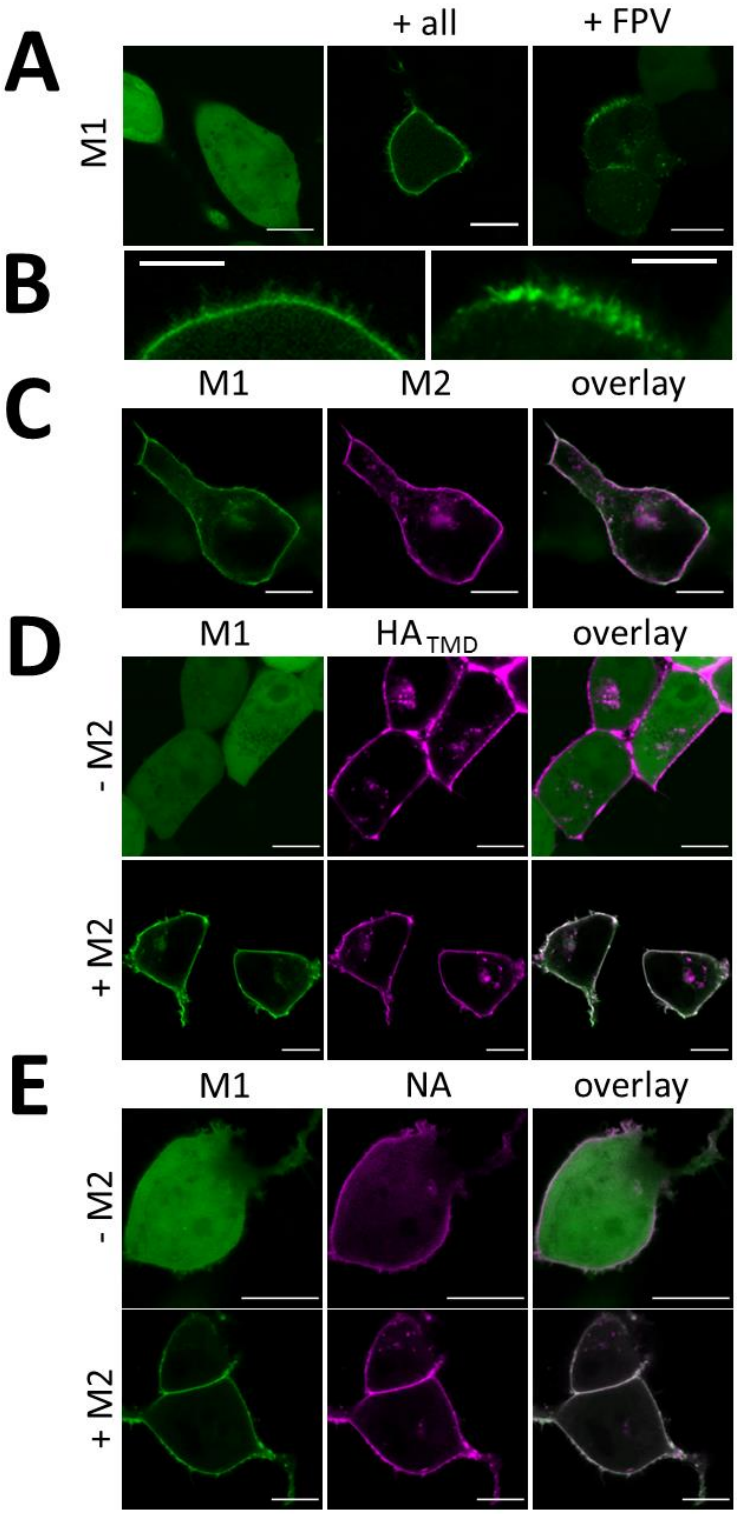

441

442 **Figure 1 Membrane recruitment of IAV matrix protein 1 (M1) in co-transfected and infected cells.** A-B: Representative
443 confocal fluorescence images of HEK293T cells expressing M1-mEGFP (green) from the influenza A/FPV/Rostock/1934 strain
444 (FPV) alone (A, left panel). The same construct was also observed in cells co-transfected with the reverse genetic plasmid
445 system of FPV "all" (A, middle; B, left) and in cells infected with FPV (A, right; B, left). C: Representative confocal
446 fluorescence images of HEK293T cells co-expressing M1-mEGFP (green) and the FPV matrix protein 2 (mCherry2-M2,
447 magenta). The right panels show the two channels merged in a single image. D: Representative confocal fluorescence
448 images of HEK293T cells co-expressing M1-mEGFP (green) and the hemagglutinin (mCherry2-HA_{TMD}, magenta) in the
449 absence (upper panels) or in the presence (lower panels) of unlabeled M2. E: Representative confocal fluorescence images
450 of HEK293T cells co-expressing M1-mEGFP (green) and the neuraminidase (NA-mCherry2, magenta) in the absence (upper
451 panels) or in the presence (lower panels) of unlabeled M2. Scale bars represent 10 µm.

bioRxiv preprint doi: https://doi.org/10.1101/2021.05.06.442926; this version posted May 7, 2021. The copyright holder for this preprint (which was not certified by peer review) is the author/funder, who has granted bioRxiv a license to display the preprint in perpetuity. It is made available under aCC-BY-NC-ND 4.0 International license.

M1 multimeric state at the PM ranges from dimers to large multimers

In order to quantify the concentration-dependent oligomerization of M1, N&B analysis was carried out in infected as well as co-transfected cells (Figure 2). This approach was applied in the past to quantify protein multimerization as a function of local concentration and cellular localization [67, 68]. Compared to other methods based on fluorescence fluctuation analysis, N&B provides more representative results in samples characterized by spatial inhomogeneities and slow dynamics [50]. The amount of fluorescence signal detected for a single independent protein complex (e.g., a protein dimer) in the unit of time is indicated by the molecular brightness. This parameter is directly connected to the number of fluorophores within such a complex and, therefore, to the multimeric state of the fusion-labeled protein. Specifically, the multimerization can be quantified by normalization of the measured brightness values with the molecular brightness of a monomeric and dimeric reference (see Material and Methods) [42].

In this context, the fluorescent construct M1-mEGFP described in the previous paragraph was expressed in HEK293T cells either i) in the presence of unlabeled M2, ii) concurrently with the reverse genetic plasmid system “all”, iii) concurrently with FPV infection or iv) alone (Figure 2).

The results shown in Figure 2 A and B indicate that, upon co-expression of M2, M1-mEGFP does not form large complexes, compared to the case in which other viral proteins are present (i.e., in the case of the reverse genetic plasmid system - named “all” henceforth - or of infection). In the latter cases, higher intensity and brightness values are in fact observed at the PM. The average intensity and molecular brightness values were calculated at each pixel of ROIs (including e.g., the PM or cytosolic regions) and represented as two dimensional histograms (Figure S2, representative example of data from Figure 2 A and B). The brightness values of M1-mEGFP within each cell were usually symmetrically distributed around their average values for co-transfected cells expressing unlabeled M2, but slightly skewed towards large values in infected cells or cells transfected with the plasmid set “all”. The brightness values of such distributions were then normalized using the corresponding monomer and dimer controls (Figure 2C). The analysis of cells expressing only M1 indicated that M1-mEGFP in the cytosol has a normalized brightness between 1 and 2 (1.2 ± 0.7,

bioRxiv preprint doi: https://doi.org/10.1101/2021.05.06.442926; this version posted May 7, 2021. The copyright holder for this preprint (which was not certified by peer review) is the author/funder, who has granted bioRxiv a license to display the preprint in perpetuity. It is made available under aCC-BY-NC-ND 4.0 International license.

median ± IQR, n = 48 cells). For comparison, the oligomerization state of control monomers (mEGFP) and dimers (mEGFP-mEGFP) is also shown. It is worth noting that N&B analysis provides an average oligomerization value in the case of mixtures of different multimeric species [68]. Therefore, the measured normalized brightness for cytosolic M1-mEGFP suggests that the protein is present as a mixture of e.g. monomers (ca. 80 %, assuming p_f = 0.7) and dimers (ca. 20 %) at the observed concentrations. M1-mEGFP oligomerization slightly increased upon binding to the PM in the presence of unlabeled M2 (2.2 ± 0.6, median ± IQR, n = 53 cells). M1-mEGFP oligomeric state increased significantly upon co-transfection with all other viral proteins ("all", 5.0 ± 1.6, median ± IQR, n = 39 cells), or upon infection (7.2 ± 5.2, median ± IQR, n = 46 cells). For comparison, the oligomeric state of control monomers (mp-mEGFP) and dimers (mp-mEGFP-mEGFP) is also shown. Additionally, M1-mEGFP showed a significant concentration-dependent oligomerization behavior in concurrently infected cells and in transfected cells expressing all other viral proteins (Figure 2 D). On the other hand, the oligomerization of M1-mEGFP in co-transfected cells expressing unlabeled M2 seemed to be independent from concentration and stable around values corresponding, in average, to M1-mEGFP dimers. As also evident from Figure 2 D, higher concentrations of M1-mEGFP at the PM were observed in general in infected cells, as well as in co-transfected cells expressing all other viral proteins. Of note, it must be considered that in infected cells, M1 concentration and oligomerization are underestimated, due to the co-expression of viral unlabeled M1 which might take part in the formation of complexes with M1-mEGFP. Since N&B analysis accounts only for labeled proteins, complexes containing both labeled and unlabeled species will effectively appear as smaller oligomers.

In summary, M1-mEGFP forms up to dimers in the cytoplasm or at the PM, upon co-expression of M2. The oligomerization of membrane-bound M1-mEGFP increases dramatically as a function of local concentration in infected cells and, to a minor extent, in cells expressing all other viral proteins via a reverse genetic plasmid system.

bioRxiv preprint doi: https://doi.org/10.1101/2021.05.06.442926; this version posted May 7, 2021. The copyright holder for this preprint (which was not certified by peer review) is the author/funder, who has granted bioRxiv a license to display the preprint in perpetuity. It is made available under aCC-BY-NC-ND 4.0 International license.

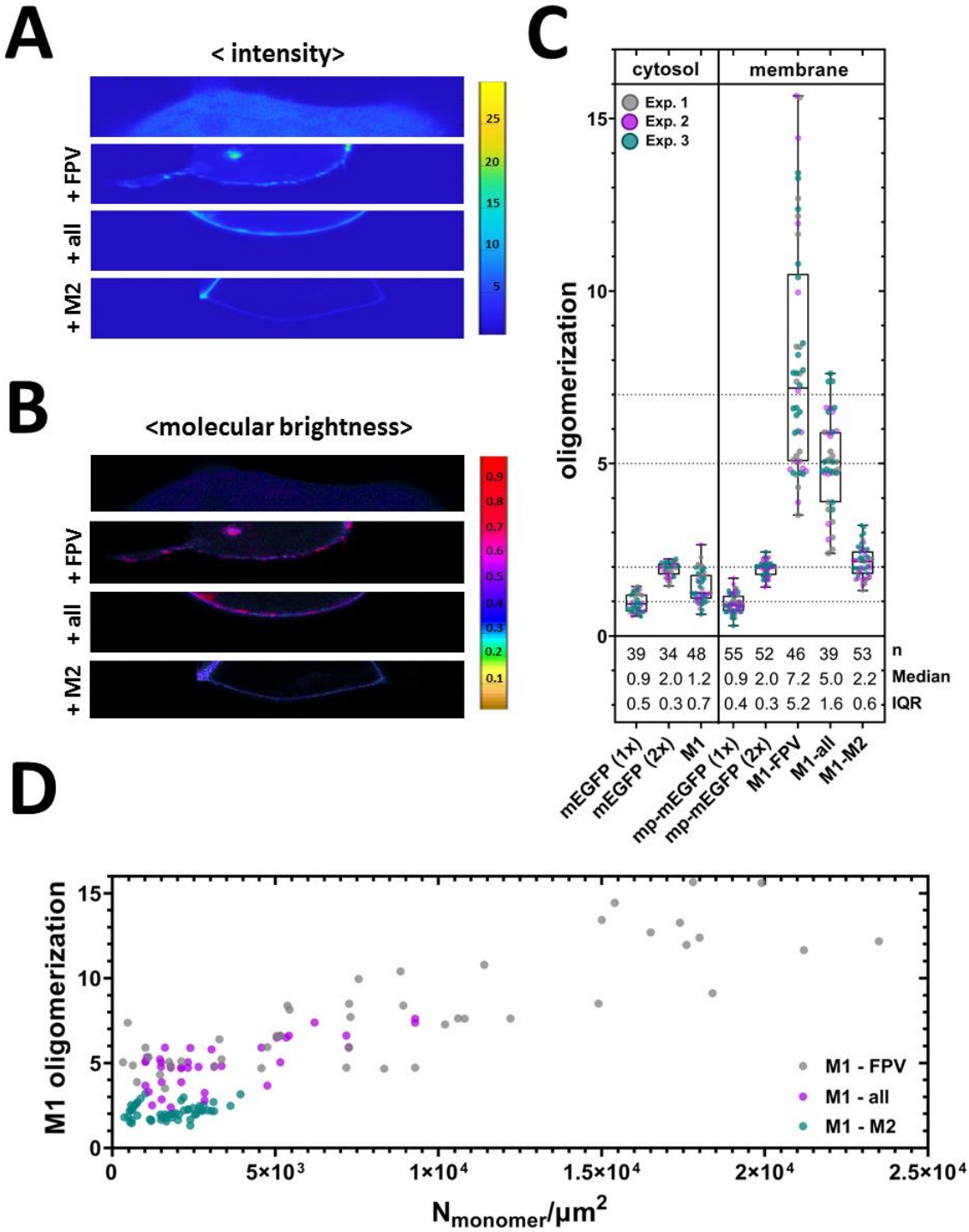

Figure 2 M1 oligomerizes in a concentration-dependent manner. Number and Brightness (N&B) analysis of M1-mEGFP in cells expressing only M1-mEGFP, infected with FPV ("+FPV"), co-transfected cells expressing unlabeled M2 and the reverse genetic plasmid system for all other FPV proteins ("+ all"), or co-transfected cells expressing unlabeled M2 ("+M2"). Oligomerization and surface concentration values were obtained as described in the Methods section. A: Representative average intensity maps of M1-mEGFP in HEK293T cells. The average intensity map is visualized via color scale with units photon counts/dwell time. B: Representative brightness-intensity maps corresponding to the images represented in panel A. The images show pixel brightness as pixel color (counts/dwell time per molecule) and mean photon count rate as pixel

bioRxiv preprint doi: https://doi.org/10.1101/2021.05.06.442926; this version posted May 7, 2021. The copyright holder for this preprint (which was not certified by peer review) is the author/funder, who has granted bioRxiv a license to display the preprint in perpetuity. It is made available under aCC-BY-NC-ND 4.0 International license.

intensity. C (left): Box plot of single data points from three independent experiments showing the normalized brightness (i.e. oligomerization) for M1-mEGFP and the corresponding controls (i.e., cytosolic monomer mEGFP (1x), cytosolic dimer mEGFP (2x) in the cytosol of HEK293T cells. C (right): Box plot of single data points from three independent experiments showing the oligomerization of M1-mEGFP at the PM of infected (M1-FPV) or co-transfected (M1-all, M1-M2) cells. Oligomerization values for PM-anchored controls (monomer mp-mEGFP(1x), dimer mp-mEGFP(2x)) are also shown. Sample size, median, and interquartile range (IQR) are indicated at the bottom. Horizontal dotted lines corresponding to oligomerization values 1, 2, 5 and 7 are shown as guide to the eye. D: M1-mEGFP oligomerization as a function of surface concentration at the PM (in $N_{monomer}/\mu m^2$). The number of replicates were: M1-FPV (n = 46), M1-all (n = 39), and M1-M2 (n = 53).

HA and NA do not induce M1 oligomerization

The interaction of M1 with other viral membrane proteins (HA, NA, and M2) is controversially discussed in previous studies [10, 11, 22-24, 30, 31, 35, 36].

To clarify this issue, we performed 2-color sFCCS analysis in HEK293T cells expressing M1-mEGFP in combination with i) mCherry2-M2, ii) mCherry2-HA_{TMD} and unlabeled M2, or iii) NA-mCherry2 and unlabeled M2. As shown in Figure 3 A for the case of co-transfected cells expressing M1-mEGFP, mCherry2-HA_{TMD}, and unlabeled M2, M1 partitions strongly at the PM. The confocal detection volume is scanned in a linear fashion perpendicularly to the PM, as illustrated by the yellow arrow. Following the calculation of ACFs and CCFs, (Figure S3), this approach allows the quantification of the interactions between two differently labeled proteins by calculating the relative cross-correlation (rel. cc), i.e. a measure of the relative abundance of molecular hetero-complexes. Furthermore, from the analysis of the ACF, sFCCS provides quantitative information about diffusion dynamics and, similar to N&B analysis, the average oligomerization state of the monitored proteins.

Our results suggest that M1 forms monomers and dimers at the PM, upon co-expression of M2 (1.7 ± 0.8, median ± IQR, n = 32 cells), confirming the results of the N&B experiments (Figure 3 B). For comparison, the oligomerization state of control monomers (mp-mEGFP) and dimers (mp-mEGFP-mEGFP) is also shown. Further, the oligomerization of M1 is not significantly altered by additionally co-expressing the IAV glycoproteins, mCherry2-HA_{TMD} (1.5 ± 0.6, median ± IQR, n = 46 cells) or NA-mCherry2 (1.5 ± 0.8, median ± IQR, n = 36 cells). To verify whether the FP fused to viral glycoproteins alters their quaternary structure, the molecular brightness of mCherry2-HA_{TMD} and NA-mCherry2 was also analyzed and compared to the corresponding controls (Figure 3 C). The HA transmembrane domain construct mCherry2-HA_{TMD} formed in average dimers (2.1 ± 0.6, median ± IQR, n = 46 cells), and NA–

bioRxiv preprint doi: https://doi.org/10.1101/2021.05.06.442926; this version posted May 7, 2021. The copyright holder for this preprint (which was not certified by peer review) is the author/funder, who has granted bioRxiv a license to display the preprint in perpetuity. It is made available under aCC-BY-NC-ND 4.0 International license.

mCherry2 formed in average tetramers (3.9 ± 0.6, median ± IQR, n = 36 cells). Both oligomeric states are consistent with those obtained in earlier studies [69, 70]. The average oligomerization state of mCherry2-M2 (3.3 ± 1.0, median ± IQR, n = 32 cells) indicated that M2 might be present as a mixture of e.g. dimers and tetramers on the PM, which is consistent with previous results [71]. Surprisingly, for all the examined IAV proteins, we observed that their average oligomerization state was not strongly influenced by their local concentration (Figure S4).

It is worth noting that the mCherry2-M2 construct (i.e., with mCherry2 fused to the N-terminus of M2) was newly designed to monitor M1:M2 interactions while avoiding steric hindrance at the cytosolic side of M2. In order to determine whether this fluorescent M2 construct behaves as expected (especially in the context of M1-M2 interactions), we used an alternative strategy to simultaneously express untagged M2 and a membrane marker (mp-mCherry2) via a bi-directional vector system (indicated as M2 ↔ mp-mCherry2) [46]. The measured concentration of mp-mCherry2 can be then used to estimate the amount of unlabeled M2 in the PM (see Materials and Methods, Figure S1). The correct expression of M2 at the PM was validated by immunofluorescence (Figure S1 C). No significant difference in the oligomeric state of M1-mEGFP as a function of the surface concentration of M2 between both plasmid constructs (i.e., bidirectional M2 and mCherry2-M2) was observed (Figure S1 D). Therefore, only the mCherry2-M2 construct was used for further investigations of M1-M2 interaction. Notably, the oligomerization of M1-mEGFP was consistently independent from the concentration of mCherry2-M2 at the PM (Figure S1 D), but correlated with the oligomerization state of mCherry2-M2 (Figure 3 D). Also, the concentration of M1-mEGFP at the PM increased with increasing mCherry2-M2 concentration (Figure 3 E). As shown in Figure 3 F, we could finally estimate that both M1-mEGFP concentration at the PM and oligomerization are circa half of what is observed for mCherry2-M2 ($M2:M1_{oligo.state}$: 2.0 ± 0.8, and $M2:M1_{surface\ conc.}$: 2.29 ± 1.16, median ± IQR).

In summary, our results suggest that M1 binds to the PM as dimer upon co-expression of M2. M1-M1 and M1-lipid interactions did not appear to be modulated by the presence of HA or NA.

bioRxiv preprint doi: https://doi.org/10.1101/2021.05.06.442926; this version posted May 7, 2021. The copyright holder for this preprint (which was not certified by peer review) is the author/funder, who has granted bioRxiv a license to display the preprint in perpetuity. It is made available under aCC-BY-NC-ND 4.0 International license.

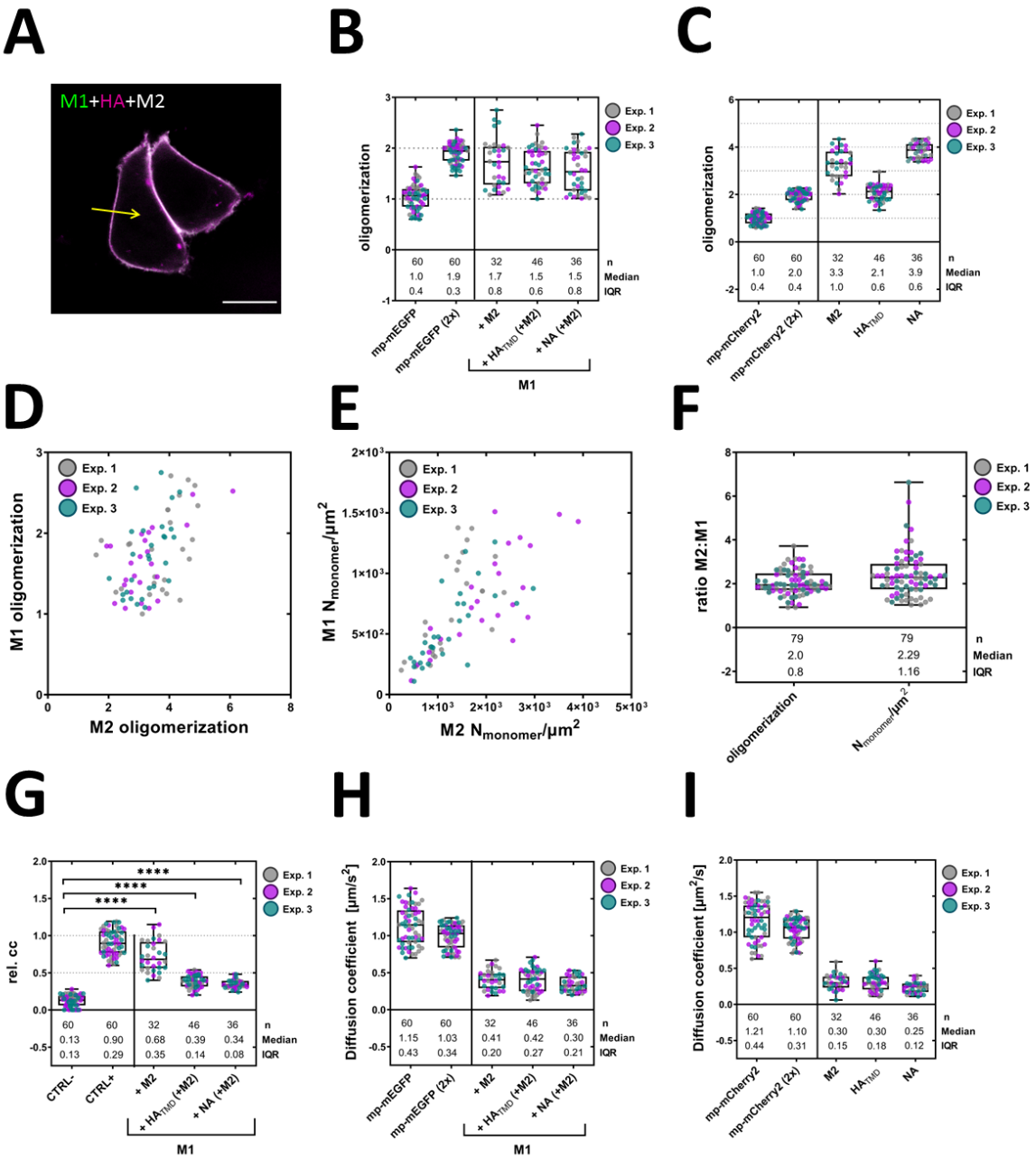

Figure 3 M2 interacts with M1 in a concentration-dependent manner. Scanning fluorescence cross-correlation spectroscopy (sFCCS) of M1-mEGFP in HEK293T cells co-expressing mCherry2-M2, mCherry2-HA$_{TMD}$/M2-untagged, and NA-mCherry2/M2-untagged. Oligomerization, surface concentration ($N_{monomer}$/µm^2), cross-correlation, and diffusion coefficient (µm^2/s) values were obtained as described in the Methods section. A: Representative confocal fluorescence image of HEK293T cells co-expressing M1-mEGFP (green), mCherry2-HA$_{TMD}$ (magenta), M2-untagged. Yellow arrow indicates the scanning path used for sFCCS. Scale bar is 10 µm. B: Box plot with single data points from three independent experiments shows the oligomerization of the controls (monomer mp-mEGFP(1x) and dimer mp-mEGFP(2x)), and M1-mEGFP under co-expression of mCherry2-M2, mCherry2-HA$_{TMD}$ /M2-untagged, and NA-mCherry2/M2-untagged. Sample size, median, and IQR are indicated in the graph. C: Box plot with single data points from three independent experiments shows the oligomerization of the controls (monomer mp-mCherry2(1x) and dimer mp-mCherry2(2x)), and the viral surface proteins mCherry2-M2, mCherry2-HA$_{TMD}$, and NA-mCherry2 under co-expression of M1-mEGFP with or without unlabeled M2. Sample size, median, and IQR are indicated in the graph. D-E: Scatter plots show the oligomerization of M1-mEGFP as a function of the oligomerization of mCherry2-M2 (D), and the surface concentration of M1-mEGFP as a function of the surface concentration of mCherry2-M2 (E). F: Box plot with single data points from three independent experiments shows the ratio of the oligomerization, and the surface concentration of M2:M1. Sample size, median, and IQR are indicated in the graph. G: Box plot with single data points from three independent experiments shows the relative cross-correlation (rel. cc) of the controls (negative control mp-mEGFP(1x)/mp-Cherry2 and positive control mp-mCherry2-mEGFP), and M1-mEGFP

bioRxiv preprint doi: https://doi.org/10.1101/2021.05.06.442926; this version posted May 7, 2021. The copyright holder for this preprint (which was not certified by peer review) is the author/funder, who has granted bioRxiv a license to display the preprint in perpetuity. It is made available under aCC-BY-NC-ND 4.0 International license.

under co-expression of mCherry2-M2, mCherry2-HA$_{TMD}$/M2-untagged, and NA-mCherry2/M2-untagged. Sample size, median, and IQR are indicated in the graph. Statistical significance was determined using one-way ANOVA multiple comparison test (**** indicates P < 0.0001 compared to the negative control (CTRL-)). H: Box plot with single data points from three independent experiments shows the diffusion coefficient of the controls (monomer mp-mEGFP(1x) and dimer: mp-mEGFP(2x)), and M1-mEGFP under co-expression of mCherry2-M2, mCherry2-HA$_{TMD}$ /M2-untagged, and NA-mCherry2/M2-untagged. Sample size, median, and IQR are indicated in the graph. I: Box plot with single data points from three independent experiments shows the diffusion coefficient of the controls (monomer mp-mCherry2(1x) and dimer mp-mCherry2(2x)), and the viral surface proteins mCherry2-M2, mCherry2-HA$_{TMD}$, and NA-mCherry2 under co-expression M1-mEGFP with or without unlabeled M2. Sample size, median, and IQR are indicated in the graph.

M1 strongly interacts with M2 but only weakly associates to HA or NA

Direct information regarding the formation of protein hetero-complexes at the PM can be derived by the analysis of ACFs and CCFs obtained via sFCCS (see previous paragraph). We therefore calculated the rel. cc as a measure of the hetero-interactions between M1-mEGFP and either mCherry2-M2, mCherry2-HA$_{TMD}$, or NA-mCherry2 (Figure 3 G, and S3). Two interacting molecules diffusing together through the observation volume as a complex will give rise to a positive rel. cc that can be quantified by the amplitude of the cross-correlation curve (Figure S3 B). Low rel. cc indicates the absence of interaction between the observed proteins (see e.g., Figure S3 A). However, due to incomplete maturation of the fluorescent proteins and the partial overlap of the confocal volumes in both channels, the maximum achievable rel. cc value is lower than 1. For example, a tandem of mp-mEGFP-mCherry2 used here as a positive control for rel. cc displayed a rel. cc of 0.90 ± 0.29 (median ± IQR, n = 60 cells). As expected, we detected a very low rel. cc (0.13 ± 0.13, median ± IQR, n = 60 cells) in negative control experiments (i.e., in samples of co-transfected cells expressing mp-mEGFP and mp-mCherry2). As shown in Figure 3 G, a rel. cc of 0.7 ± 0.4 (median ± IQR, n = 32 cells) was measured for M1-mEGFP co-expressed with mCherry2-M2. This value is significantly higher than the negative control and close to that obtained for the positive control, suggesting very strong association of (ca. 80%, after normalization to the positive control and assuming a simple scenario consisting of M1 dimers, M2 tetramers and 2:4 M1-M2 complexes) M1-mEGFP with mCherry2-M2.

On the other hand, the obtained rel. cc values for M1-mEGFP co-expressed with either mCherry2-HA$_{TMD}$, or NA-mCherry2 (rel. cc(M1,HA$_{TMD}$) = 0.39 ± 0.14, n = 46 cells; rel. cc(M1,NA) = 0.34 ± 0.08, n = 36 cells, median ± IQR) were lower but still significantly higher than the negative control. It is worth noting that such measurements could only be performed in the presence of unlabeled M2 since, without this third protein, no localization

bioRxiv preprint doi: https://doi.org/10.1101/2021.05.06.442926; this version posted May 7, 2021. The copyright holder for this preprint (which was not certified by peer review) is the author/funder, who has granted bioRxiv a license to display the preprint in perpetuity. It is made available under aCC-BY-NC-ND 4.0 International license.

of M1-mEGFP at the PM could be observed (see previous paragraphs). The observed rel. cc values indicate a weak interaction between M1-mEGFP and the glycoproteins mCherry2-HA_{TMD}, and NA-mCherry2. To further investigate this issue, we quantified the interaction between M1 and the glycoproteins also in infected cells. To this aim, we performed ccN&B in cells infected with FPV and, additionally, co-transfected with M1-mEGFP and either mCherry2-HA_{TMD} or NA-mCherry2 plasmids. Similar to sFCCS, ccN&B can be used to quantify the rel. cc between different FPs, especially in samples characterized by slow dynamics [50]. Scanning FCCS measurements of M1-mEGFP in infected cells did not provide in fact reproducible results (data not shown). As shown in Figure S5, the rel. cc values determined by ccN&B in infected cells for M1-mEGFP and mCherry2-HA_{TMD} (rel. cc(M1,HA_{TMD}) = 0.31 ± 0.10, n = 21 cells, median ± IQR), as well as for M1-mEGFP and NA-mCherry2 (rel. cc(M1,NA) = 0.28 ± 0.08, n = 22 cells, median ± IQR) were similar to the rel. cc values obtained in non-infected cells, as measured via sFCCS (Figure 3 G).

Finally, we quantified protein dynamics by fitting a two-dimensional diffusion model to the ACF data (Figure 3 H and I, S3). Knowing the size of the observation volume, it is possible to obtain diffusion coefficients of the proteins (D in $\mu m/s^2$, see Material and Methods). Protein diffusion depends in general on the size of the protein complex and on protein-membrane interactions. The diffusion coefficients measured for M1-mEGFP at the PM (D=0.3-0.4 $\mu m/s^2$, Figure 3 H) were lower than those of the monomer control (D = 1.1 ± 0.4 $\mu m/s^2$, median ± IQR, n = 60), and similar to the diffusion coefficient of the IAV integral surface proteins mCherry2-M2, mCherry2-HA_{TMD}, and NA-mCherry2 (indicated in Figure 3 I).

Taken together, our data indicate that M1 strongly interacts with M2. On the other hand, a relatively small amount of complexes containing M1 together with HA or NA was detected.

Non-specific M1 recruitment to the PM is sufficient for the establishment of M1-HA interaction

To investigate the origin of the interaction between M1 and HA (or NA) which was observed in cells additionally expressing M2, we artificially induced M1 binding to the PM. These experiments were performed to test the hypothesis that M1 is recruited (by M2) to the PM, where it can then interact with other membrane proteins (independently from the specific protein that first induced M1-PM binding).

bioRxiv preprint doi: https://doi.org/10.1101/2021.05.06.442926; this version posted May 7, 2021. The copyright holder for this preprint (which was not certified by peer review) is the author/funder, who has granted bioRxiv a license to display the preprint in perpetuity. It is made available under aCC-BY-NC-ND 4.0 International license.

Specifically, we designed two M1 constructs in which the protein was modified by myristoylation and palmitoylation (mp-M1-mEGFP) and, additionally, with a poly-lysine motif (mp-KrΦ-M1-mEGFP), as shown in Figure 4 A. The underlying idea is that the additional targeting sequences direct M1 specifically to lipid ordered "raft" domains (mp motif) or to "non-raft" regions containing acidic lipids (poly-lysine motifs) in the PM, as supported by previous studies [27, 45, 72, 73]. The viral envelope proteins HA, and NA were previously reported to localize in lipid "rafts", whereas M2 was observed at the edges of lipid rafts [7, 14].

First, we verified the sub-localization of the two new constructs in transfected HEK293T cells. Both, mp-M1-mEGFP and mp-KrΦ-M1-mEGFP, were efficiently trafficked to the PM (Figure 4 B). Next, we examined the rel. cc between these two constructs and mCherry2-HA_{TMD}, as well as NA-mCherry2 (Figure 4 C) in co-transfected cells. The obtained rel. cc values (indicated in Figure 4 C) for mp-M1-mEGFP with mCherry2-HA_{TMD} or NA-mCherry2, as well as mp-KrΦ-M1-mEGFP with NA-mCherry2, were similar to those of the negative rel. cc control. These results indicate that NA-mCherry2 does not significantly interact with any of the modified membrane-associated M1 constructs. Also, mCherry2-HA_{TMD} does not seem to interact with the supposedly lipid raft-associated mp-M1-mEGFP. In contrast, a reproducible interaction between mp-KrΦ-M1-mEGFP and mCherry2-HA_{TMD} (rel. cc(mp-KrΦ-M1,HA_{TMD}) = 0.26 ± 0.18, n = 30 cells, median ± IQR) was observed. Notably, the rel. cc value observed in this case was significantly lower than the one obtained in the context of the interaction between (wildtype) M1-mEGFP and mCherry2-HA_{TMD}, in the presence of M2. Next, we calculated the surface concentration of each protein and plotted the cross-correlation values against the surface concentration, as well as the ratio of the concentration between the protein pairs (Figure S6). This analysis was performed to exclude that the obtained rel. cc values are influenced by the surface concentration of the proteins or the expression ratio between the proteins. No concentration-dependency of the rel. cc for all pairs was observed.

Finally, we quantified the diffusion dynamics of the examined protein constructs (Figure 4 D). The obtained diffusion coefficient values (shown in Figure 4 D) for mp-M1-mEGFP in the presence of mCherry2-HA_{TMD} or NA-mCherry2 were similar to those of the monomer control (mp-mEGFP). A similar observation was made for mp-KrΦ-M1-mEGFP in the presence of NA-mCherry2. The fact these M1 constructs diffuse as fast as a lipid-anchored protein (rather

bioRxiv preprint doi: https://doi.org/10.1101/2021.05.06.442926; this version posted May 7, 2021. The copyright holder for this preprint (which was not certified by peer review) is the author/funder, who has granted bioRxiv a license to display the preprint in perpetuity. It is made available under aCC-BY-NC-ND 4.0 International license.

that a membrane-spanning protein, see Figure 3 I) suggest the absence of significant interactions/co-diffusion of these M1 constructs with mCherry2-HA_{TMD} or NA-mCherry2. For comparison, the diffusion coefficients of M1-mEGFP in the presence of M2 and one glycoprotein are also reported in Figure 4 D (D = 0.38 ± 0.23 µm/s^2, median ± IQR, n = 46, when co-expressed e.g. with mCherry2-HA_{TMD}). This result is comparable to the diffusion coefficient of mCherry2-M2 (D = 0.30 ± 0.15 µm/s^2, median ± IQR, n = 46, Figure 3 I). Interestingly, the diffusion coefficient for mp-KrΦ-M1-mEGFP (D = 0.60 ± 0.16 µm/s^2, median ± IQR, n = 32) co-expressed with mCherry2-HA_{TMD} was lower than that measured for the monomer control, although still higher than the one measured for M1-mEGFP in the presence of unlabeled M2.

In conclusion, NA-mCherry2 does not exhibit significant cross-correlation or co-diffusion with neither of the “artificially” PM-associated M1 proteins. In contrast, mCherry2-HA_{TMD} appears to interact with M1 depending on the specific way in which the latter is anchored to the PM.

bioRxiv preprint doi: https://doi.org/10.1101/2021.05.06.442926; this version posted May 7, 2021. The copyright holder for this preprint (which was not certified by peer review) is the author/funder, who has granted bioRxiv a license to display the preprint in perpetuity. It is made available under aCC-BY-NC-ND 4.0 International license.

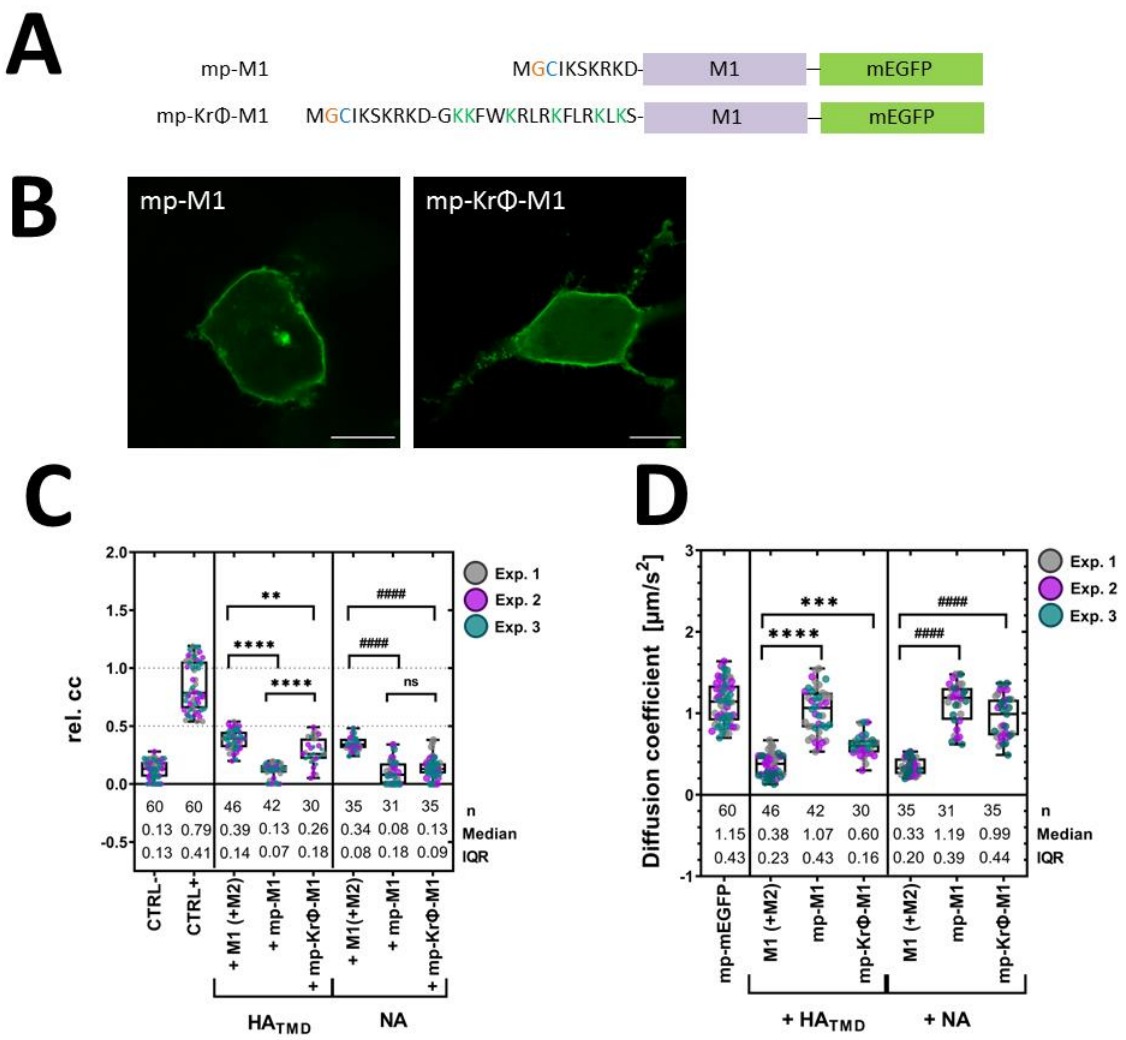

Figure 4 HA interacts with a membrane-associated M1 construct. A: Schematic diagram of M1 expression constructs with N-terminal PM-targeting sequences. One construct has a myristoylation (orange) and palmitoylation (blue) motif (mp-M1-mEGFP), and the other on has an additional poly-lysine motif (green letters, mp-KrΦ-M1-mEGFP), which are targeting sequences for lipid raft regions, and lipid-raft/non-raft border zones in the PM, respectively. B: Representative M1 subcellular localization images in transfected HEK293T cells expressing mp-M1-mEGFP (left side), or mp-KrΦ-M1-mEGFP (right side). Scale bars represent 10 µm. C: Box plot with single data points from three independent experiments shows the cross-correlation of the controls (negative control mp-mEGFP(1x)/mp-mCherry2(1x) and positive control mp-mCherry2-mEGFP), and M1-mEGFP, mp-M1-mEGFP, and mp-KrΦ-M1-mEGFP under co-expression of mCherry2-HA_{TMD}, or NA-mCherry2. Sample size, median, and IQR are indicated in the graph. Statistical significance was determined using one-way ANOVA multiple comparison test (** indicates $p < 0.01$, **** indicates $p < 0.0001$ compared to M1-mEGFP/ mCherry2-HA_{TMD}; #### indicates $p < 0.0001$ compared to M1-mEGFP/ NA-mCherry2, ns indicates not significant). D: Box plot with single data points from three independent experiments shows the diffusion coefficient of the monomer control (mp-mEGFP), and M1-mEGFP, mp-M1-mEGFP, and mp-KrΦ-M1-mEGFP under co-expression of mCherry2-HA_{TMD}, or NA-mCherry2. Sample size, median, and IQR are indicated in the graph. Statistical significance was determined using one-way ANOVA multiple comparison test (*** indicates $p < 0.001$, **** indicates $p < 0.0001$ compared to M1-mEGFP/ mCherry2-HA_{TMD}; #### indicates $p < 0.0001$ compared to M1-mEGFP/ NA-mCherry2).

bioRxiv preprint doi: https://doi.org/10.1101/2021.05.06.442926; this version posted May 7, 2021. The copyright holder for this preprint (which was not certified by peer review) is the author/funder, who has granted bioRxiv a license to display the preprint in perpetuity. It is made available under aCC-BY-NC-ND 4.0 International license.

A potential M2 binding site is located in the N-domain (aa 1-67) of M1.

An interaction site for M2 has not been yet identified within M1. Therefore, we created different M1 constructs for the expression of specific protein subdomains, in order to locate a potential M2 binding site (Figure 5 A). The truncated M1 constructs encoded i) the entire M1 N-terminus (NM1, amino acids 1–164), ii) only the N-terminus domain with the linker region (NM1, amino acids 1–86), iii) only the N-terminus domain (NM1, amino acids 1–63) or iv) the M1 C-terminus (CM1, amino acids 165–252). A mEGFP was fused to the C-terminal site of each M1 variants. Moreover, a well conserved amino acid sequence in the cytoplasmic C-terminal tail of M2 at the position 71 and 73 was previously shown as an interaction site for M1 [10, 11]. Hence, we generated a substitution mutant of M2 ($M2_{mut}$) in which the triplet sequence (71 – SMR – 73) was replaced by alanine (Figure 5 A).

To verify whether the truncated M1-mEGFP constructs are altered in their subcellular localization, we observed them in HEK293T in the absence of mCherry2-M2. All truncated M1-mEGFP variants showed a similar subcellular localization to the wildtype M1-mEGFP (Figure 1 A, and 5 B). Next, all truncated M1-mEGFP constructs were co-expressed with mCherry2-M2 in HEK293T cells. All N-terminus M1 variants were recruited to the PM whereas the C-terminus M1 construct showed still a homogeneous distribution in the cytoplasm (Figure 5 C). The percentages of cells with M1 at the PM for the NM1 variants were similar as observed for the M1 wildtype in co-expression with mCherry2-M2 (data not shown). These results indicated that the M2 binding site might be pinpointed to the N-terminal domain of M1 and, specifically, to the amino acids 1-63. Furthermore, no recruitment of M1 wildtype was observed upon a co-expression with the mCherry2-$M2_{mut}$ (Figure 5 D). Based on this result, we could confirm that the recruitment of M1 to PM occurred via a specific interaction of M1 with the amino acid sequence (71 – SMR – 73) on M2.

bioRxiv preprint doi: https://doi.org/10.1101/2021.05.06.442926; this version posted May 7, 2021. The copyright holder for this preprint (which was not certified by peer review) is the author/funder, who has granted bioRxiv a license to display the preprint in perpetuity. It is made available under aCC-BY-NC-ND 4.0 International license.

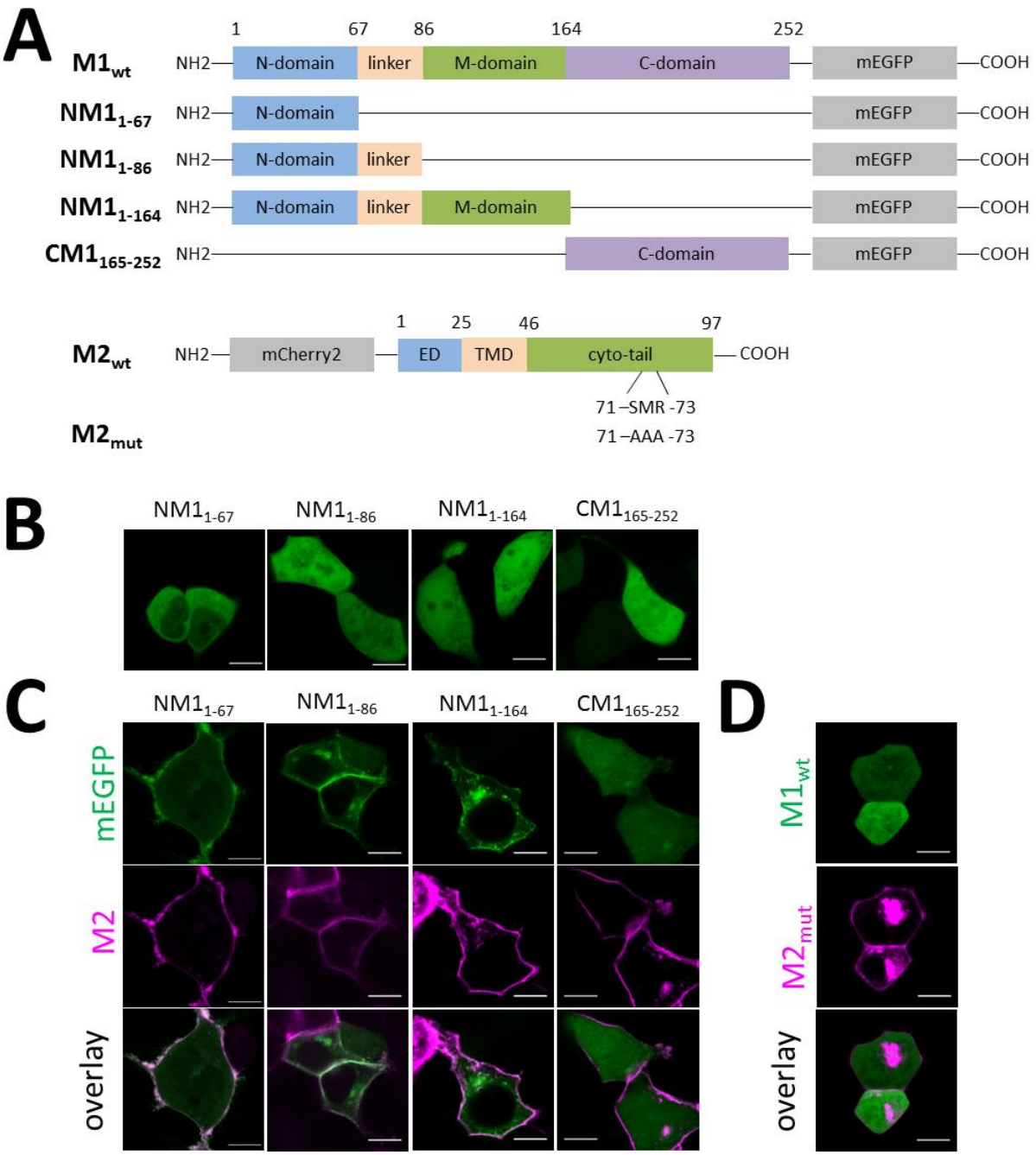

Figure 5 M2 binding site on M1 is located in the N-terminus domain. A: Schematic diagram of different M1 and M2 expression constructs. On top, M1 constructs showing the wildtype and the truncated M1 variants with their domains: N-terminus domain (N-domain, aa 1-67, blue), linker region (orange, aa 68-86), middle domain (M-domain, aa 87-164, green), and C-terminus domain (C-domain, aa 165-252, purple). A mEGFP was fused to the C-terminus of each species. On the bottom, M2 constructs showing the wildtype and the M2 mutant (71-SMR-73 was replaced by three alanine) with their domains: ectodomain (ED, aa 1-25, blue), transmembrane domain (TMD, aa 26-46, orange), cytoplasmic tail (cyto-tail, aa 47-97, green). Each construct had a mCherry2 fused to the N-terminal site of M2. B: Representative confocal fluorescence images of HEK293T cells expressing truncated M1-mEGFP variants: $NM1_{1-67}$, $NM1_{1-86}$, $NM1_{1-164}$, and $CM1_{165-252}$. C: Representative confocal fluorescence images of HEK293T cells expressing truncated M1-mEGFP variants: $NM1_{1-67}$, $NM1_{1-86}$, $NM1_{1-164}$, and $CM1_{165-252}$ (green) with wildtype mCherry2-M2 (magenta). (D) Representative confocal fluorescence images of HEK293T cells expressing wildtype M1-mEGFP (green) with mCherry2-M2 mutant ($M2_{mut}$, magenta). Scale bars represent 10 µm.

bioRxiv preprint doi: https://doi.org/10.1101/2021.05.06.442926; this version posted May 7, 2021. The copyright holder for this preprint (which was not certified by peer review) is the author/funder, who has granted bioRxiv a license to display the preprint in perpetuity. It is made available under aCC-BY-NC-ND 4.0 International license.

Discussion

The role of M1 in IAV assembly is of fundamental importance, as it is now understood that this protein connects together the viral envelope, its membrane proteins (HA, NA, and M2) and the genome [74]. It has been suggested that interactions of M1 with the viral glycoproteins (e.g. HA) drive M1 localization to the PM of infected cells [10, 11, 22-24], but other studies reported conflicting data regarding the interaction of M1 with HA and NA [30, 31, 35, 36]. Such findings are mostly based on biochemistry approaches providing indirect interaction data [7, 75].

Therefore, in order to quantify protein-protein interactions directly at the PM of living cells, we performed fluorescence fluctuation spectroscopy experiments under physiological conditions. Such experimental approaches (i.e., sF(C)CS and (cc)N&B) provide information regarding the oligomeric state, surface concentration, hetero-interactions and dynamics in complex biological systems [50, 55, 68, 76-78].

To this aim, we selected HEK293T cells as a cellular model because they are often used for reverse genetic virus production [40, 41, 79], were shown to be appropriate for IAV protein expression [17, 42, 43] and are better suited for quantitative fluorescence fluctuation analysis of proteins at the PM, compared to other cell lines [80]. Additionally, we produced and tested several fluorescent IAV protein constructs. Of note, the fluorescent NA construct designed in this study allowed for the first time the investigation of the interaction between this IAV glycoprotein and other viral proteins directly in living cells. It is worth noting that incorporating fluorescent fusion tags might have an impact in general on the localization, function, and conformation of the protein of interest [81, 82]. For example, our control experiments showed that the cellular distribution of M1 with an mEGFP fused to its C-terminus was similar to that of unlabeled M1 [44, 63], whereas an N-terminally fused mEGFP M1 variant seemed to have transport failures which are probably caused by steric hindrance between fluorophore and signal peptide [44]. On the other hand, the fluorescent constructs used to investigate the viral envelope proteins (HA, NA, and M2) were all localized at the PM, similar to the corresponding non-fluorescent proteins [65, 66], and yielded the expected oligomerization state [42, 43, 69, 70]. For example, our results are compatible with the presence of NA tetramers and mixtures of M2 dimers and tetramers (Figure 3C), in

bioRxiv preprint doi: https://doi.org/10.1101/2021.05.06.442926; this version posted May 7, 2021. The copyright holder for this preprint (which was not certified by peer review) is the author/funder, who has granted bioRxiv a license to display the preprint in perpetuity. It is made available under aCC-BY-NC-ND 4.0 International license.

agreement with previous data [71, 83]. Furthermore, we also demonstrated that the protein-protein interactions investigated here (e.g. between M1-mEGFP and mCherry2-M2) are specific and analogous to those observed in other contexts [10], as shown by mutagenesis experiments (Figure 5D) and using unlabeled interaction partners (Figure S1).

In order to identify the minimum requirement for M1 association to the PM, we observed cells expressing different combinations of viral proteins. First, we confirmed that M1 does not bind to the PM in the absence of other viral proteins, despite the observation of strong lipid-protein interactions previously observed in model membrane systems [17-20]. Surprisingly, we did not observe any recruitment of M1 to the PM in the presence of HA or NA (Figure 1). It is worth noting that several studies proposed that M1 interacts with the cytoplasmic tails of HA or NA [23, 30, 84-87], but our direct observations in living cells strongly suggest that the two IAV glycoproteins are not able to recruit M1 to the PM by themselves. It is unlikely that the lack of interaction might be a simple consequence of the presence of fluorescent labels, since HA and NA are labeled at the extracellular side. Also, the same M1-mEGFP strongly associates with the PM in the presence of M2. This result is in agreement with previous studies indicating that M1-M2 interactions affect M1 localization and drive virus assembly [10, 11, 27, 88, 89]. For the first time, we could provide direct experimental evidence that the M2-binding region is located within the first 67 amino acids of M1 (Figure 5). Also, thanks to the application of quantitative fluorescence microscopy methods, we could additionally prove that M1 and M2 do not simply colocalize at the PM but rather form complexes. This conclusion is supported by the similar diffusion dynamics observed for M1 and M2 (i.e. diffusion coefficients typical of trans-membrane proteins rather than membrane-associated proteins, Figure 3 H) and by the significant degree of cross-correlation between the signals of the two proteins (Figure 3 G). M1-M2 complexes appear to consist, in average, of 1-2 M1 and 2-4 M2 molecules (Figure 3). Assuming that each M2 monomer has a binding site for M1, the observed 1:2 stoichiometry suggests that the M1 binding might be limited for example by steric constraints or competition with other binding partners of M2 (e.g., LC3 [43]). Furthermore, in the simple approximation of M1 dimers, M2 tetramers, and 2:4 M1-M2 complexes being associated to the PM, our cross-correlation measurements indicate that ca. 80% of M1 is indeed complexed to M2. The remaining amount of PM-associated M1 might interact with e.g. acidic lipids at the PM [19,

bioRxiv preprint doi: https://doi.org/10.1101/2021.05.06.442926; this version posted May 7, 2021. The copyright holder for this preprint (which was not certified by peer review) is the author/funder, who has granted bioRxiv a license to display the preprint in perpetuity. It is made available under aCC-BY-NC-ND 4.0 International license.

20] but, of note, we never observed any significant degree of M1 localization at the PM in the absence of M2. This finding puts forward the hypothesis that M2-M1 complex formation might facilitate the interaction of M1 with other membrane components. This mechanism might also explain previous findings indicating the presence of HA and M1 in the same membrane fractions [22, 23] or within the same region in the PM [15]. Accordingly, we have observed that in the presence of M2 (i.e. M1 being efficiently recruited to the PM) there is a significant (although modest) interaction between M1 and the glycoproteins HA or NA (Figure 3 G). On one hand, it is possible that e.g. M1-HA interactions are not direct but, rather, mediated by M2 [15]. Alternatively, it is possible that, while M2 is needed for the initial recruitment of M1 to the PM, M1-M2 interactions are not long-lived and can be partially replaced for example by M1-HA interactions. In this case, M2 might induce interactions between M1 and other membrane components by e.g. increasing M1 local concentration in specific PM regions or stabilizing a certain geometric configuration of M1. Based on control experiments monitoring M1-HA/NA interactions as a function of local protein concentration (Figure S6), a prominent role of concentration seems unlikely though. To evaluate whether M2 is strictly needed for HA-M1 interactions, we performed sFCCS experiments in which M1 was artificially anchored to the PM (Figure 4). In this case, depending on the specific lipid anchor, we were able to observe M1-HA interactions also in the absence of M2, thus indicating that i) the latter protein is not always required as a bridge between M1 and IAV glycoproteins and ii) the lipid environment plays a role in the establishment of interactions among IAV proteins. Of interest, it was shown that HA is associated to specific lipids, such as PI(4,5)P2 [14, 66] and this observation might provide a molecular mechanism explaining our observation of non-negligible M1-HA interactions, in the case that M1 was artificially anchored to the membrane via lipidation and, additionally, a polybasic motif. The degree of association between HA and mp-KrΦ-M1-mEGFP appeared to be between that observed for wt M1 and that observed for mp-M1-mEGFP, as supported by the observation of intermediate cross-correlation values (Figure 4 C) and diffusion dynamics (Figure 4 D).

The observation that one single IAV membrane protein (i.e. M2) is sufficient for the recruitment of M1 to the PM prompted us to investigate whether M1-M2 interaction is also sufficient for the initiation of the large-scale M1 multimerization associated with IAV

bioRxiv preprint doi: https://doi.org/10.1101/2021.05.06.442926; this version posted May 7, 2021. The copyright holder for this preprint (which was not certified by peer review) is the author/funder, who has granted bioRxiv a license to display the preprint in perpetuity. It is made available under aCC-BY-NC-ND 4.0 International license.

assembly [17]. Our experiments clearly demonstrate that this is not the case, since M1 remains, in average, mostly dimeric when bound to the PM in the presence of M2 (Figure 2 C). On the other hand, in the presence of all the other viral proteins, M1 formed larger multimers (up to 5-10 monomers). This effect does not seem to be a direct consequence of the presence of HA or NA alone (Figure 3B) and is even stronger in infected cells. It is worth noting that the formation of very large multimers of M1-mEGFP in infected cells might be partially due to the presence of unlabeled M1 molecules which more efficiently support protein-protein interactions. It was in fact reported that fluorescent viral proteins might not be able to oligomerize on a very large scale [55]. Alternatively, other viral proteins or altered lipid metabolism (and, consequently, modification of PM composition) in infected cells might play a role and these possibilities are currently under investigation.

In conclusion, our study sheds light on the very first steps in IAV assembly. According to our results, the main role of M2 in this context is to recruit M1 to specific regions of the PM. This is in agreement with previously proposed models according to which M2 chaperones M1 to the PM [90] and, specifically, to interface regions between “raft” and “non-raft” domains [14, 16] or domains enriched in negatively-charged lipids [17]. In further steps, M1 can then interact with lipids and other viral proteins and such interactions might be involved in the formation of larger protein complexes eventually leading to IAV capsid assembly.

Acknowledgments

This work was supported by the German Research Foundation (DFG grant #254850309 to S.C.).

Author contributions

Research planning, A.P. and S.C; investigation, A.P.; data analysis, A.P.; writing-original draft preparation, A.P. and S.C.; writing-review and editing, V.D. and S.B.; software, V.D. and S.C.; supervision, S.C.; funding acquisition, S.C.

bioRxiv preprint doi: https://doi.org/10.1101/2021.05.06.442926; this version posted May 7, 2021. The copyright holder for this preprint (which was not certified by peer review) is the author/funder, who has granted bioRxiv a license to display the preprint in perpetuity. It is made available under aCC-BY-NC-ND 4.0 International license.

Reference

1. Davlin, S., et al., *Influenza Activity - United States, 2015-16 Season and Composition of the 2016-17 Influenza Vaccine.* MMWR. Morbidity and mortality weekly report, 2016. **65**: p. 567-575.
2. Taubenberger, J.K. and D.M. Morens, *Pandemic influenza--including a risk assessment of H5N1.* Revue scientifique et technique (International Office of Epizootics), 2009. **28**(1): p. 187-202.
3. Bouvier, N.M. and P. Palese, *The biology of influenza viruses.* Vaccine, 2008. **26 Suppl 4**(Suppl 4): p. D49-D53.
4. Taubenberger, J.K. and J.C. Kash, *Influenza virus evolution, host adaptation, and pandemic formation.* Cell host & microbe, 2010. **7**(6): p. 440-451.
5. Mostafa, A., et al., *Zoonotic Potential of Influenza A Viruses: A Comprehensive Overview.* Viruses, 2018. **10**(9): p. 497.
6. Samji, T., *Influenza A: understanding the viral life cycle.* The Yale journal of biology and medicine, 2009. **82**(4): p. 153-159.
7. Veit, M. and B. Thaa, *Association of influenza virus proteins with membrane rafts.* Adv Virol, 2011. **2011**: p. 370606.
8. Dou, D., et al., *Influenza A Virus Cell Entry, Replication, Virion Assembly and Movement.* Front Immunol, 2018. **9**: p. 1581.
9. Manzoor, R., M. Igarashi, and A. Takada, *Influenza A Virus M2 Protein: Roles from Ingress to Egress.* Int J Mol Sci, 2017. **18**(12).
10. Chen, B.J., et al., *The influenza virus M2 protein cytoplasmic tail interacts with the M1 protein and influences virus assembly at the site of virus budding.* Journal of virology, 2008. **82**(20): p. 10059-10070.
11. McCown, M.F. and A. Pekosz, *Distinct domains of the influenza a virus M2 protein cytoplasmic tail mediate binding to the M1 protein and facilitate infectious virus production.* Journal of virology, 2006. **80**(16): p. 8178-8189.
12. Rossman, J.S., et al., *Influenza virus m2 ion channel protein is necessary for filamentous virion formation.* Journal of virology, 2010. **84**(10): p. 5078-5088.
13. Rossman, J.S., et al., *Influenza virus M2 protein mediates ESCRT-independent membrane scission.* Cell, 2010. **142**(6): p. 902-913.
14. Veit, M., et al., *Lipid domain association of influenza virus proteins detected by dynamic fluorescence microscopy techniques.* Cell Microbiol, 2013. **15**(2): p. 179-89.
15. Leser, G.P. and R.A. Lamb, *Lateral Organization of Influenza Virus Proteins in the Budozone Region of the Plasma Membrane.* J Virol, 2017. **91**(9).
16. Rossman, J.S. and R.A. Lamb, *Influenza virus assembly and budding.* Virology, 2011. **411**(2): p. 229-36.
17. Bobone, S., et al., *Phosphatidylserine Lateral Organization Influences the Interaction of Influenza Virus Matrix Protein 1 with Lipid Membranes.* Journal of virology, 2017. **91**(12): p. e00267-17.
18. Dahmani, I., K. Ludwig, and S. Chiantia, *Influenza A matrix protein M1 induces lipid membrane deformation via protein multimerization.* Biosci Rep, 2019. **39**(8).
19. Hilsch, M., et al., *Influenza A matrix protein M1 multimerizes upon binding to lipid membranes.* Biophys J, 2014. **107**(4): p. 912-23.

bioRxiv preprint doi: https://doi.org/10.1101/2021.05.06.442926; this version posted May 7, 2021. The copyright holder for this preprint (which was not certified by peer review) is the author/funder, who has granted bioRxiv a license to display the preprint in perpetuity. It is made available under aCC-BY-NC-ND 4.0 International license.

20. Höfer, C.T., et al., *Structural determinants of the interaction between influenza A virus matrix protein M1 and lipid membranes.* Biochim Biophys Acta Biomembr, 2019. **1861**(6): p. 1123-1134.
21. Noton, S.L., et al., *Identification of the domains of the influenza A virus M1 matrix protein required for NP binding, oligomerization and incorporation into virions.* J Gen Virol, 2007. **88**(Pt 8): p. 2280-2290.
22. Barman, S., et al., *Transport of viral proteins to the apical membranes and interaction of matrix protein with glycoproteins in the assembly of influenza viruses.* Virus Research, 2001. **77**(1): p. 61-69.
23. Jin, H., et al., *Influenza virus hemagglutinin and neuraminidase cytoplasmic tails control particle shape.* The EMBO journal, 1997. **16**(6): p. 1236-1247.
24. Zhang, J., A. Pekosz, and R.A. Lamb, *Influenza virus assembly and lipid raft microdomains: a role for the cytoplasmic tails of the spike glycoproteins.* Journal of virology, 2000. **74**(10): p. 4634-4644.
25. Darapaneni, V., *Large-scale Analysis of Influenza A Virus Sequences Reveals Universally Conserved Residues of Matrix Proteins.* American Journal of Current Microbiology, 2015. **3**: p. 1-13.
26. Nayak, D.P., et al., *Influenza virus morphogenesis and budding.* Virus Res, 2009. **143**(2): p. 147-61.
27. Wang, D., et al., *The Lack of an Inherent Membrane Targeting Signal Is Responsible for the Failure of the Matrix (M1) Protein of Influenza A Virus To Bud into Virus-Like Particles.* Journal of Virology, 2010. **84**(9): p. 4673.
28. Ruigrok, R.W., et al., *Membrane interaction of influenza virus M1 protein.* Virology, 2000. **267**(2): p. 289-98.
29. Baudin, F., et al., *In vitro dissection of the membrane and RNP binding activities of influenza virus M1 protein.* Virology, 2001. **281**(1): p. 102-8.
30. Ali, A., et al., *Influenza virus assembly: effect of influenza virus glycoproteins on the membrane association of M1 protein.* Journal of virology, 2000. **74**(18): p. 8709-8719.
31. Enami, M. and K. Enami, *Influenza virus hemagglutinin and neuraminidase glycoproteins stimulate the membrane association of the matrix protein.* Journal of virology, 1996. **70**(10): p. 6653-6657.
32. Su, W.-C., et al., *Ubiquitination of the Cytoplasmic Domain of Influenza A Virus M2 Protein Is Crucial for Production of Infectious Virus Particles.* Journal of virology, 2018. **92**(4): p. e01972-17.
33. García-Sastre, A. and P. Palese, *The cytoplasmic tail of the neuraminidase protein of influenza A virus does not play an important role in the packaging of this protein into viral envelopes.* Virus Res, 1995. **37**(1): p. 37-47.
34. Jin, H., G.P. Leser, and R.A. Lamb, *The influenza virus hemagglutinin cytoplasmic tail is not essential for virus assembly or infectivity.* EMBO J, 1994. **13**(22): p. 5504-15.
35. Kretzschmar, E., M. Bui, and J.K. Rose, *Membrane Association of Influenza Virus Matrix Protein Does Not Require Specific Hydrophobic Domains or the Viral Glycoproteins.* Virology, 1996. **220**(1): p. 37-45.
36. Zhang, J. and R.A. Lamb, *Characterization of the Membrane Association of the Influenza Virus Matrix Protein in Living Cells.* Virology, 1996. **225**(2): p. 255-266.
37. Chen, B.J., et al., *Influenza virus hemagglutinin and neuraminidase, but not the matrix protein, are required for assembly and budding of plasmid-derived virus-like particles.* Journal of virology, 2007. **81**(13): p. 7111-7123.

bioRxiv preprint doi: https://doi.org/10.1101/2021.05.06.442926; this version posted May 7, 2021. The copyright holder for this preprint (which was not certified by peer review) is the author/funder, who has granted bioRxiv a license to display the preprint in perpetuity. It is made available under aCC-BY-NC-ND 4.0 International license.

38. Liu, H., M.L. Grantham, and A. Pekosz, *Mutations in the Influenza A Virus M1 Protein Enhance Virus Budding To Complement Lethal Mutations in the M2 Cytoplasmic Tail.* Journal of virology, 2017. **92**(1): p. e00858-17.
39. Dunsing, V. and S. Chiantia, *A Fluorescence Fluctuation Spectroscopy Assay of Protein-Protein Interactions at Cell-Cell Contacts.* JoVE, 2018(142): p. e58582.
40. Wagner, R., et al., *Protease activation mutants elicit protective immunity against highly pathogenic avian influenza viruses of subtype H7 in chickens and mice.* Emerging microbes & infections, 2013. **2**(2): p. e7-e7.
41. Wagner, R., et al., *Acylation-Mediated Membrane Anchoring of Avian Influenza Virus Hemagglutinin Is Essential for Fusion Pore Formation and Virus Infectivity.* Journal of Virology, 2005. **79**(10): p. 6449.
42. Dunsing, V., et al., *Optimal fluorescent protein tags for quantifying protein oligomerization in living cells.* Scientific reports, 2018. **8**(1): p. 10634-10634.
43. Dunsing, V., A. Petrich, and S. Chiantia, *Multi-color fluorescence fluctuation spectroscopy in living cells via spectral detection.* bioRxiv, 2020: p. 2020.12.18.423407.
44. Thaa, B., A. Herrmann, and M. Veit, *The polybasic region is not essential for membrane binding of the matrix protein M1 of influenza virus.* Virology, 2009. **383**(1): p. 150-155.
45. Zacharias, D.A., et al., *Partitioning of Lipid-Modified Monomeric GFPs into Membrane Microdomains of Live Cells.* Science, 2002. **296**(5569): p. 913.
46. Orekhova, A.S., et al., *[Novel bidirectional promoter from human genome].* Mol Biol (Mosk), 2011. **45**(3): p. 486-95.
47. Baer, A. and K. Kehn-Hall, *Viral concentration determination through plaque assays: using traditional and novel overlay systems.* Journal of visualized experiments : JoVE, 2014(93): p. e52065-e52065.
48. Petrášek, Z. and P. Schwille, *Precise Measurement of Diffusion Coefficients using Scanning Fluorescence Correlation Spectroscopy.* Biophysical Journal, 2008. **94**(4): p. 1437-1448.
49. Bacia, K., S.A. Kim, and P. Schwille, *Fluorescence cross-correlation spectroscopy in living cells.* Nature Methods, 2006. **3**(2): p. 83-89.
50. Dunsing, V., et al., *Direct evidence of amyloid precursor-like protein 1 trans interactions in cell-cell adhesion platforms investigated via fluorescence fluctuation spectroscopy.* Molecular biology of the cell, 2017. **28**(25): p. 3609-3620.
51. Schneider, F., et al., *Diffusion of lipids and GPI-anchored proteins in actin-free plasma membrane vesicles measured by STED-FCS.* Molecular biology of the cell, 2017. **28**(11): p. 1507-1518.
52. Ries, J. and P. Schwille, *Studying Slow Membrane Dynamics with Continuous Wave Scanning Fluorescence Correlation Spectroscopy.* Biophysical Journal, 2006. **91**(5): p. 1915-1924.
53. Ries, J., S. Chiantia, and P. Schwille, *Accurate determination of membrane dynamics with line-scan FCS.* Biophysical journal, 2009. **96**(5): p. 1999-2008.
54. Digman, M.A., et al., *Stoichiometry of molecular complexes at adhesions in living cells.* Proceedings of the National Academy of Sciences of the United States of America, 2009. **106**(7): p. 2170-2175.
55. Petazzi, R.A., et al., *Detection of Envelope Glycoprotein Assembly from Old-World Hantaviruses in the Golgi Apparatus of Living Cells.* J Virol, 2020.

bioRxiv preprint doi: https://doi.org/10.1101/2021.05.06.442926; this version posted May 7, 2021. The copyright holder for this preprint (which was not certified by peer review) is the author/funder, who has granted bioRxiv a license to display the preprint in perpetuity. It is made available under aCC-BY-NC-ND 4.0 International license.

56. Linkert, M., et al., *Metadata matters: access to image data in the real world.* Journal of Cell Biology, 2010. **189**(5): p. 777-782.
57. Digman, M.A., et al., *Mapping the number of molecules and brightness in the laser scanning microscope.* Biophys J, 2008. **94**(6): p. 2320-32.
58. Trullo, A., et al., *Application limits and data correction in number of molecules and brightness analysis.* Microscopy Research and Technique, 2013. **76**(11): p. 1135-1146.
59. Chen, Y., et al., *Chapter 16 - Observing Protein Interactions and Their Stoichiometry in Living Cells by Brightness Analysis of Fluorescence Fluctuation Experiments*, in *Methods in Enzymology*, N.G. Walter, Editor. 2010, Academic Press. p. 345-363.
60. Wickham, H., *ggplot2 - Elegant Graphics for Data Analysis*. 2nd ed. 2016, New York: Springer International Publishing.
61. Kassambara, A. *ggpubr: 'ggplot2' Based Publication Ready Plots. R package version 0.4.0.* https://CRAN.R-project.org/package=ggpubr. 2020.
62. Wilke, C.O. *cowplot: Streamlined Plot Theme and Plot Annotations for 'ggplot2'. R package version 1.1.0.* https://CRAN.R-project.org/package=cowplot. 2020.
63. Das, S.C., et al., *The highly conserved arginine residues at positions 76 through 78 of influenza A virus matrix protein M1 play an important role in viral replication by affecting the intracellular localization of M1.* Journal of virology, 2012. **86**(3): p. 1522-1530.
64. Hoffmann, E., et al., *"Ambisense" approach for the generation of influenza A virus: vRNA and mRNA synthesis from one template.* Virology, 2000. **267**(2): p. 310-7.
65. Chlanda, P., et al., *Structural Analysis of the Roles of Influenza A Virus Membrane-Associated Proteins in Assembly and Morphology.* J Virol, 2015. **89**(17): p. 8957-66.
66. Curthoys, N.M., et al., *Influenza Hemagglutinin Modulates Phosphatidylinositol 4,5-Bisphosphate Membrane Clustering.* Biophys J, 2019. **116**(5): p. 893-909.
67. Digman, M.A., et al., *Mapping the Number of Molecules and Brightness in the Laser Scanning Microscope.* Biophysical Journal, 2008. **94**(6): p. 2320-2332.
68. Petazzi, R.A., A.K. Aji, and S. Chiantia, *Chapter One - Fluorescence microscopy methods for the study of protein oligomerization*, in *Progress in Molecular Biology and Translational Science*, J. Giraldo and F. Ciruela, Editors. 2020, Academic Press. p. 1-41.
69. Scolari, S., et al., *Lateral distribution of the transmembrane domain of influenza virus hemagglutinin revealed by time-resolved fluorescence imaging.* The Journal of biological chemistry, 2009. **284**(23): p. 15708-15716.
70. Varghese, J.N., W.G. Laver, and P.M. Colman, *Structure of the influenza virus glycoprotein antigen neuraminidase at 2.9 Å resolution.* Nature, 1983. **303**(5912): p. 35-40.
71. Georgieva, E.R., et al., *Mechanism of influenza A M2 transmembrane domain assembly in lipid membranes.* Scientific reports, 2015. **5**: p. 11757-11757.
72. Gao, X. and J. Zhang, *Spatiotemporal analysis of differential Akt regulation in plasma membrane microdomains.* Molecular biology of the cell, 2008. **19**(10): p. 4366-4373.
73. Yeung, T., et al., *Receptor Activation Alters Inner Surface Potential During Phagocytosis.* Science, 2006. **313**(5785): p. 347.
74. Nayak, D.P., E.K. Hui, and S. Barman, *Assembly and budding of influenza virus.* Virus Res, 2004. **106**(2): p. 147-65.
75. Zhao, H. and P. Lappalainen, *A simple guide to biochemical approaches for analyzing protein-lipid interactions.* Molecular biology of the cell, 2012. **23**(15): p. 2823-2830.

bioRxiv preprint doi: https://doi.org/10.1101/2021.05.06.442926; this version posted May 7, 2021. The copyright holder for this preprint (which was not certified by peer review) is the author/funder, who has granted bioRxiv a license to display the preprint in perpetuity. It is made available under aCC-BY-NC-ND 4.0 International license.

76. Dawes, M.L., C. Soeller, and S. Scholpp, *Studying molecular interactions in the intact organism: fluorescence correlation spectroscopy in the living zebrafish embryo.* Histochem Cell Biol, 2020. **154**(5): p. 507-519.
77. Langowski, J., *Protein-protein interactions determined by fluorescence correlation spectroscopy.* Methods Cell Biol, 2008. **85**: p. 471-84.
78. Tzoneva, R., et al., *Effect of Erufosine on Membrane Lipid Order in Breast Cancer Cell Models.* Biomolecules, 2020. **10**(5).
79. Hoffmann, E., et al., *A DNA transfection system for generation of influenza A virus from eight plasmids.* Proceedings of the National Academy of Sciences of the United States of America, 2000. **97**(11): p. 6108-6113.
80. Dunsing, V., *Fluorescence fluctuation spectroscopy techniques to quantify molecular interactions and dynamics in complex biological systems*. 2020, University of Potsdam: Faculty of Science - Institute for Physics and Astronomy. p. 164.
81. Rana, M.S., X. Wang, and A. Banerjee, *An Improved Strategy for Fluorescent Tagging of Membrane Proteins for Overexpression and Purification in Mammalian Cells.* Biochemistry, 2018. **57**(49): p. 6741-6751.
82. Snapp, E., *Design and use of fluorescent fusion proteins in cell biology.* Current protocols in cell biology, 2005. **Chapter 21**: p. 21.4.1-21.4.13.
83. Cristian, L., J.D. Lear, and W.F. DeGrado, *Use of thiol-disulfide equilibria to measure the energetics of assembly of transmembrane helices in phospholipid bilayers.* Proc Natl Acad Sci U S A, 2003. **100**(25): p. 14772-7.
84. Barman, S., et al., *Role of transmembrane domain and cytoplasmic tail amino acid sequences of influenza a virus neuraminidase in raft association and virus budding.* Journal of virology, 2004. **78**(10): p. 5258-5269.
85. Zhang, J., et al., *The cytoplasmic tails of the influenza virus spike glycoproteins are required for normal genome packaging.* Virology, 2000. **269**(2): p. 325-34.
86. Melkonian, K.A., et al., *Role of lipid modifications in targeting proteins to detergent-resistant membrane rafts. Many raft proteins are acylated, while few are prenylated.* J Biol Chem, 1999. **274**(6): p. 3910-7.
87. Tatulian, S.A. and L.K. Tamm, *Secondary structure, orientation, oligomerization, and lipid interactions of the transmembrane domain of influenza hemagglutinin.* Biochemistry, 2000. **39**(3): p. 496-507.
88. Iwatsuki-Horimoto, K., et al., *The cytoplasmic tail of the influenza A virus M2 protein plays a role in viral assembly.* J Virol, 2006. **80**(11): p. 5233-40.
89. McCown, M.F. and A. Pekosz, *The influenza A virus M2 cytoplasmic tail is required for infectious virus production and efficient genome packaging.* J Virol, 2005. **79**(6): p. 3595-605.
90. Zebedee, S.L. and R.A. Lamb, *Growth restriction of influenza A virus by M2 protein antibody is genetically linked to the M1 protein.* Proc Natl Acad Sci U S A, 1989. **86**(3): p. 1061-5.